
FOGO: Forgetting-aware Orthogonalization Optimizer

Toan Nguyen

School of Computer Science and Engineering
University of New South Wales
Sydney, Australia
toan.nguyen@unsw.edu.au

Yang Liu

School of Computer Science and Engineering
University of New South Wales
Sydney, Australia
yang.liu39@student.unsw.edu.au

Trung Le

Department of Data Science & AI
Monash University
Melbourne, Australia
trunglm@monash.edu

Celso De Melo

DEVCOM Army Research Laboratory
USA
celso.miguel.de.melo@gmail.com

Flora D. Salim *

School of Computer Science and Engineering
University of New South Wales
Sydney, Australia
flora.salim@unsw.edu.au

Abstract

We argue that forgetting is not confined to continual learning but is a general optimization phenomenon: during standard training, dominant mini-batch gradients suppress rare but useful update directions, causing short-term forgetting at every step. When such knowledge is never revisited, these losses compound into long-term forgetting—the classical failure mode of continual learning. We introduce FOGO, a scalable optimizer that continuously detects and resolves gradient interference across both regimes. FOGO spectrally orthogonalizes momentum updates to prevent dominant directions from monopolizing optimization, then stores representative past directions in a compact codebook memory built on random projection, where pairwise distances are provably preserved in low-dimensional space. At each step, conflicts between the current update and stored directions are resolved via lightweight orthogonal correction and lifted back through a proximal step, with minimal overhead and no data storage. Across class-imbalanced classification, continual visual learning under domain and class shifts, continual fine-tuning of LLaVA-7B, and GPT-2 pretraining, FOGO consistently improves convergence and knowledge retention, outperforming Adam and Muon.

1 Introduction

Deep learning has achieved remarkable progress across vision [17], language [34], and multimodal tasks [41], yet its dominant training paradigm struggles when knowledge must be retained and accumulated over time. Humans naturally integrate new experiences without overwriting old ones; neural networks, optimized under stationary regimes, lack this ability and degrade under distribution

*Corresponding Author.

shift. Continual learning formalizes this challenge [7], but despite substantial progress, a fundamental gap remains.

Continual learning has largely been studied as a problem separate from standard training, with distinct benchmarks, methods, and metrics. Recent work has begun to narrow this divide: Abel et al. [1] reinterpret continual learning as continual adaptation, while gradient-interference analyses show that forgetting arises when new updates overwrite parameter directions useful for prior knowledge [11, 35]. We push this further and argue that *all* learning is a continual process of resolving interference between incoming and existing knowledge. Under this lens, standard training and task-sequential continual learning are not separate problems but different regimes of the same phenomenon. In standard training, dominant mini-batch gradients can suppress rare but useful directions, causing *short-term forgetting* at each optimization step. When such knowledge is not revisited, these losses accumulate into *long-term forgetting*—the classical failure mode of continual learning. We validate this through controlled experiments on class-imbalanced CIFAR-10: short-term forgetting exists and degrades underrepresented classes. Random batching mitigates it in common balanced settings—explaining why it has been overlooked—but fails under imbalance or distribution shift.

This unified view calls for a unified optimizer. We introduce FOGO, a scalable optimizer that continuously detects and resolves gradient conflicts across both forgetting regimes. FOGO combines two mechanisms. First, it spectrally orthogonalizes momentum updates, preventing dominant directions from monopolizing optimization and exposing rare but informative components. Second, it stores useful update directions in a compact codebook memory. Using random projection—inspired by recent work on data diversity measurement [24]—FOGO maps high-dimensional updates to a low-dimensional space where pairwise distances are approximately preserved [22], maintains representative directions as centroids, and resolves conflicts via lightweight orthogonal correction before lifting the result back through a proximal step. This yields an optimizer-level memory that operates entirely in projected space, keeping per-step overhead minimal.

We evaluate FOGO across a broad spectrum of settings: class-imbalanced classification, continual visual learning under domain and class shifts, LLaVA-7B fine-tuning on visual question answering, and GPT-2 pretraining. Across all settings, FOGO consistently improves retention and convergence, outperforming Adam [26] and recent matrix-aware alternatives such as Muon [23]. These results suggest that forgetting is not only a challenge of task-sequential learning but a general optimization problem—and that directional memory offers a practical route toward resolving it.

2 Related Work

2.1 Matrix-aware and Orthogonalized Optimizers

Matrix-aware optimizers have re-emerged as strong alternatives to diagonal adaptive methods [31, 39]. Shampoo [15] captures richer geometry via structured tensor preconditioning, while Muon [23] simplifies this idea by orthogonalizing momentum updates with Newton–Schulz iterations, yielding strong LLM pretraining results [31]. Recent work studies Muon through spectral-norm geometry [3] and improves it with faster polar approximations and adaptive variants [39]. FOGO goes beyond using orthogonalized updates for conditioning: it stores useful update directions in efficient codebook memories to mitigate both short-term and long-term forgetting in standard and continual learning.

2.2 Continual Learning

Continual learning is commonly formulated as a task-sequential problem, where forgetting is measured by performance degradation on previous tasks. A complementary view attributes forgetting to gradient interference [11, 32, 35], while Abel et al. [1] reframe learning as endless adaptation rather than convergence to a fixed solution. We draw on both: FOGO treats standard training and task-sequential continual learning as regimes of a single interference problem, distinguished by the source, frequency, and timescale of conflicting gradients. Among existing methods [4, 36], gradient-constrained ones are closest to ours. GEM and A-GEM [5, 32] constrain updates via reference gradients from stored examples, tying anti-forgetting to raw data retention. OGD [11] and GPM [37] avoid stored data by projecting onto orthogonal subspaces, but rely on full-rank gradient bases or SVD over high-dimensional activations. Recent optimizers such as UPGD [10] and spectral-orthogonalization methods [2, 16] address non-stationarity more directly, yet none persistently tracks

past gradient geometry to detect inter-task conflicts. FOGO closes this gap with a compact gradient memory via random projection, which provably preserves pairwise distances [22], enabling per-step interference detection without raw data or full-rank decompositions. As this memory grows only logarithmically in parameter dimension, FOGO scales naturally to the billion-parameter regime demanded by continual adaptation of large pre-trained models [21, 43].

3 Background

3.1 Muon and Orthogonalization-Based Optimizers

Given a momentum matrix $B_t \in \mathbb{R}^{m \times n}$ with compact SVD $B_t = U_t \Sigma_t V_t^\top$, the *orthogonalized update* is its polar factor $\mathcal{O}(B_t) := U_t V_t^\top$, which removes singular-value scaling while preserving directional structure. In practice, $\mathcal{O}(B_t)$ is efficiently approximated by Newton–Schulz iterations [3, 18]. Muon [23] applies this idea to matrix-valued parameters: given weight $W_t \in \mathbb{R}^{m \times n}$ and gradient $G_t = \nabla_W \mathcal{L}(W_t)$,

$$B_t = \mu B_{t-1} + G_t, \quad O_t = \text{Newton-Schulz}(B_t, T), \quad W_{t+1} = W_t - \eta O_t, \quad (1)$$

where $B_0 = \mathbf{0}$ and $\mu, \eta \in (0, 1)$. By flattening the singular spectrum, orthogonalization prevents a few dominant modes from dictating the update, letting weaker but coherent directions contribute more strongly. This perspective extends to other orthogonalization-based optimizers [2, 15] and motivates our continual optimizer for mitigating forgetting.

3.2 Orthogonalization in Continual Learning

Orthogonal gradient methods project each update onto the orthogonal complement of past-task directions to prevent interference [11, 43]. OGD [11] maintains a set S of past gradient directions and projects the current gradient as:

$$\tilde{G} = G - \sum_{G' \in S} \frac{\langle G, G' \rangle}{\langle G', G' \rangle} G'. \quad (2)$$

A key limitation is scalability: $|S|$ grows with the number of tasks, making both storage and per-step projection prohibitive for large models.

3.3 Random Projection of Gradients

Operating directly in parameter space $\mathbb{R}^{|\theta|}$ is expensive. Following recent work on gradient-space diversity measurement [12, 24], we apply a Rademacher random projection $\Pi \in \mathbb{R}^{|\theta| \times d}$, $\Pi_{ij} \sim \mathcal{U}(\{-1, 1\})$, to obtain $G_i^{\text{proj}} = \Pi^\top G_i$ with $d \ll |\theta|$. As a Johnson–Lindenstrauss transform [22], this preserves pairwise distances up to $(1 \pm \epsilon)$ distortion with high probability when $d = \mathcal{O}(\epsilon^{-2} \log N)$. The projected gradients yield a compact, geometry-preserving embedding of the gradient distribution, whose structure reveals representative update directions. We provide extended background in Appendix A.

4 Method

4.1 Why Learning is Prone to Forgetting

Motivation. Forgetting is typically framed as a consequence of task boundaries or distribution shifts [42]. We argue it is more fundamental: even in standard stochastic training, under-represented data subsets produce update directions misaligned with the dominant optimization trajectory, and their information is gradually overwritten. Forgetting is thus a *generic consequence of stochastic optimization*, not merely an artifact of task sequentiality.

Gradient mismatch. A natural measure of interference is the cosine similarity between the incoming mini-batch gradient G_t and the accumulated momentum B_{t-1} : negative values indicate that the new gradient opposes the accumulated direction. Yet this global measure can remain positive even when directions useful for under-represented data are being overwritten. To capture such fine-grained conflicts, we analyze mismatch within the dominant singular subspace of B_{t-1} .

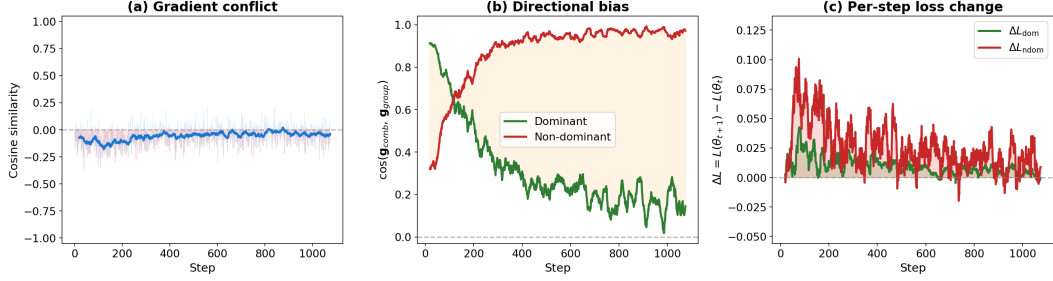


Figure 1: **Short-term forgetting under class imbalance** (CIFAR-10, ResNet-18, 5 rare classes at 10% data). (a) Dominant and rare gradients maintain negative cosine similarity throughout training. (b) The combined update initially aligns with the dominant group; after dominant loss saturates (\sim step 200), the bias reverses. (c) Per-step validation loss change on a held-out probe: the suppressed group’s loss increases after each update, confirming Theorem 1.

Dominant subspace. Transformer updates often have concentrated singular spectra [19, 38]. Let $B_{t-1} = U_{t-1} \Sigma_{t-1} V_{t-1}^\top$ be the SVD, with $U_{t-1}^{(r)}$ and $V_{t-1}^{(r)}$ containing the top- r singular vectors. The projection onto and residual from this subspace are

$$G_t^\parallel = U_{t-1}^{(r)} U_{t-1}^{(r)\top} G_t V_{t-1}^{(r)} V_{t-1}^{(r)\top}, \quad G_t^\perp = G_t - G_t^\parallel, \quad (3)$$

where G_t^\perp measures update mass outside the dominant historical directions.

Theorem 1 (Suppression of off-subspace directions). Let $\mathcal{P}_t^{(r)}(X) = U_t^{(r)} U_t^{(r)\top} X V_t^{(r)} V_t^{(r)\top}$ be the two-sided projection onto the top- r subspace of B_t , with $\mathcal{P}_t^{(r)\perp}(X) = X - \mathcal{P}_t^{(r)}(X)$. Define $R_t := \|\mathcal{P}_t^{(r)\perp}(B_t)\|_F$ and $\varepsilon_t := \|\mathcal{P}_t^{(r)\perp}(G_t)\|_F$. Under momentum update $B_t = \mu B_{t-1} + G_t$ with $\mu \in [0, 1)$, if the dominant subspace drifts slowly, $\|\mathcal{P}_t^{(r)} - \mathcal{P}_{t-1}^{(r)}\|_{F \rightarrow F} \leq \delta_t$, then

$$R_t \leq \mu R_{t-1} + \mu \delta_t \|B_{t-1}\|_F + \varepsilon_t.$$

Off-subspace mass grows only through subspace drift ($\mu \delta_t \|B_{t-1}\|_F$) and newly injected off-subspace energy (ε_t). When both are small, the residual contracts while dominant directions continue to accumulate—directions not consistently reinforced become progressively less influential.

Corollary 2 (Short-term forgetting). If, under Theorem 1, B_{s-1} is concentrated in its top- r subspace while G_s contains useful off-subspace components ($\varepsilon_s > 0$), these contribute only as small perturbations under slow subspace drift. Batch-specific directions misaligned with the accumulated trajectory are thus under-represented in B_s , causing immediate interference.

Corollary 3 (Long-term forgetting). Under Theorem 1, if later gradients provide little off-subspace energy along previously useful directions, their relative mass in the momentum state decays over time, yielding long-term forgetting.

In standard learning, stochastic mini-batching mitigates short-term forgetting through implicit replay: repeated resampling re-injects useful directions. In data-free continual learning, however, past directions cannot be reinforced once suppressed, and Theorem 1 predicts persistent long-term forgetting. We validate this on class-imbalanced CIFAR-10 [28] (Section 5.1), where five rare classes retain only 10% of their data. Fig. 1 confirms the causal chain: persistent gradient conflict (a) forces directional bias (b), causing measurable per-step loss degradation on the suppressed group (c). A detailed analysis is in Appendix F.1.

4.2 FOGO: Forgetting-aware Orthogonalization Optimizer

4.2.1 From Orthogonalization to Directional Memory

Orthogonalizing momentum preserves singular directions while flattening their spectrum, preventing high-energy modes from monopolizing the update and keeping weaker but useful directions visible

(Proposition 6, Appendix B.3). However, orthogonalization alone does not protect these directions over time: future gradients can still overwrite them, and storing raw gradients is infeasible at scale. FOGO addresses this by maintaining a compact directional memory in a low-dimensional projected space. Using random projection [22, 24], it tracks representative past directions whose pairwise geometry is preserved with high probability, then corrects each orthogonalized update to remain compatible with this memory before applying it—mitigating conflicts with controlled overhead.

4.2.2 Memory of Gradients

Slow-fast orthogonalized streams. To capture both stable and emerging directions, FOGO maintains two momentum states at different timescales. At step t , given gradient $G_t = \nabla_{\theta} \mathcal{L}_t(\theta_{t-1}) \in \mathbb{R}^{m \times n}$:

$$B_t^{(s)} = \mu_s B_{t-1}^{(s)} + G_t, \quad B_t^{(f)} = \mu_f B_{t-1}^{(f)} + G_t, \quad \mu_s > \mu_f, \quad B_t^{(s)}, B_t^{(f)} \in \mathbb{R}^{m \times n},$$

where the slow stream captures persistent trends and the fast stream tracks recent changes. Both are orthogonalized via Newton–Schulz iterations and projected into a compact d -dimensional space ($d \ll n$):

$$O_t^{(\cdot)} = \text{NEWTONSCHULZ}(B_t^{(\cdot)}; K_{(\cdot)}), \quad P_t^{(\cdot)} = O_t^{(\cdot)} \Pi \in \mathbb{R}^{m \times d},$$

where $\Pi \in \mathbb{R}^{n \times d}$ is a fixed Rademacher random matrix with entries drawn i.i.d. from $\mathcal{U}(\{-1, 1\})$. For each row i , we fuse the projected slow and fast directions via spherical interpolation ($z'_{t,i}, z_{t,i} \in \mathbb{R}^d$):

$$z'_{t,i} = \text{SLERP}(P_{t,i}^{(s)}, P_{t,i}^{(f)}; \xi), \quad z_{t,i} = \|P_{t,i}^{(s)}\|_2 z'_{t,i},$$

where ξ controls interpolation strength and the slow stream sets the scale. Stacking rows gives $Z_t = [z_{t,1}; \dots; z_{t,m}] \in \mathbb{R}^{m \times d}$. Details are in Appendix C.1.

Online directional memory. FOGO maintains a spherical codebook $\mathcal{C}_t = \{c_{t,1}, \dots, c_{t,C}\} \subset \mathbb{R}^d$ that summarizes recurring update directions. Each fused row $z_{t,i}$ is normalized to $q_{t,i} = z_{t,i} / (\|z_{t,i}\|_2 + \varepsilon)$ and assigned to its nearest centroid under cosine similarity:

$$a_{t,i}^{\text{mem}} = \arg \max_{j \in \{1, \dots, C\}} \langle q_{t,i}, \bar{c}_{t-1,j} \rangle, \quad \bar{c}_{t-1,j} = \frac{c_{t-1,j}}{\|c_{t-1,j}\|_2 + \varepsilon}.$$

Assignments are accumulated into EMA sufficient statistics and flushed after each memory-guided update to obtain \mathcal{C}_t , with centroids re-normalized onto the unit sphere. Codebook collapse is prevented via decorrelation against nearby centroids and periodic re-seeding of inactive ones (Appendix C.2).

4.2.3 Addressing Short-Term and Long-Term Forgetting

FOGO compares each orthogonalized update against its codebook of gradient centroids and corrects directions that interfere with stored memory, performing memory-guided updates that preserve plasticity while suppressing destructive interference.

Short-term angular-band filtering. Short-term forgetting arises not only from anti-aligned updates but also from repeatedly reinforcing dominant local directions. FOGO treats a near-orthogonal angular band around each pre-update centroid as locally safe and corrects updates that fall outside it.

For $q_{t,i} = z_{t,i} / (\|z_{t,i}\|_2 + \varepsilon)$, we partition centroids into over-aligned and conflicting sets:

$$\mathcal{H}_{t,i}^{\text{st}} = \{j : \langle q_{t,i}, \bar{c}_{t-1,j} \rangle > \epsilon_{\text{st}}\}, \quad \mathcal{C}_{t,i}^{\text{st}} = \{j : \langle q_{t,i}, \bar{c}_{t-1,j} \rangle < -\epsilon_{\text{st}}\}.$$

We form the projected components and subtract them:

$$z_{t,i}^{\text{hi}} = \sum_{j \in \mathcal{H}_{t,i}^{\text{st}}} \alpha_{t,i,j}^+ \langle z_{t,i}, \bar{c}_{t-1,j} \rangle \bar{c}_{t-1,j}, \quad z_{t,i}^{\text{conf}} = \sum_{j \in \mathcal{C}_{t,i}^{\text{st}}} \alpha_{t,i,j}^- \langle z_{t,i}, \bar{c}_{t-1,j} \rangle \bar{c}_{t-1,j},$$

$$\tilde{z}_{t,i} = z_{t,i} - \gamma_{\text{hi}} z_{t,i}^{\text{hi}} - \gamma_{\text{st},t} z_{t,i}^{\text{conf}}.$$

Conflicting components are explicitly removed, while over-aligned components are only mildly deflated (γ_{hi} small) as an exploration regularizer against collapse onto dominant directions. The coefficient $\gamma_{\text{st},t}$ adapts to batch-level energy outside the safe band. Weighting and scheduling details are in Appendix C.3.

Long-term near-orthogonal protection. After completing task \mathcal{T}_τ , FOGO freezes important centroids $\{\bar{c}_{\mathcal{T}_\tau, k}\}_{k=1}^{K_\tau}$ with importance weights $\{\nu_{\mathcal{T}_\tau, k}\}_{k=1}^{K_\tau}$ as long-term memory of sensitive past-task directions. At step t of the current task, updates should remain nearly orthogonal to these directions. Given the short-term corrected $\tilde{z}_{t,i}$ with $\tilde{q}_{t,i} = \tilde{z}_{t,i}/(\|\tilde{z}_{t,i}\|_2 + \varepsilon)$, we activate protection for centroids not sufficiently orthogonal:

$$\mathcal{B}_{t,i}^{\text{lt}} = \{(\mathcal{T}_\tau, k) \in \mathcal{A}_t^{\text{lt}} : |\langle \tilde{q}_{t,i}, \bar{c}_{\mathcal{T}_\tau, k} \rangle| > \epsilon_{\text{lt}}\},$$

where $\mathcal{A}_t^{\text{lt}}$ denotes available frozen centroids and $\epsilon_{\text{lt}} < \epsilon_{\text{st}}$ enforces stricter protection. The long-term correction subtracts the importance-weighted protected component:

$$z_{t,i}^{\text{lt}} = \sum_{(\mathcal{T}_\tau, k) \in \mathcal{B}_{t,i}^{\text{lt}}} \nu_{\mathcal{T}_\tau, k} \langle \tilde{z}_{t,i}, \bar{c}_{\mathcal{T}_\tau, k} \rangle \bar{c}_{\mathcal{T}_\tau, k}, \quad \tilde{z}_{t,i} = \tilde{z}_{t,i} - \gamma_{\text{lt}} z_{t,i}^{\text{lt}}.$$

Long-term memory thus acts as an importance-weighted orthogonality constraint, suppressing sensitive directions while preserving free subspaces for adaptation. Details on centroid selection, candidate sampling, and importance weighting are in Appendix C.4.

4.3 Projection Back to Original Space and Parameter Update

Memory corrections are computed in the projected space. Since $\Pi \in \mathbb{R}^{n \times d}$ is not invertible, we lift the protected direction back via a proximal least-squares problem. For row i , let $\Delta z_{t,i} = \tilde{z}_{t,i} - P_{t,i}^{(s)} \in \mathbb{R}^d$ be the projected correction relative to the slow stream. We seek the minimal high-dimensional correction consistent with $\Delta z_{t,i}$:

$$\delta_{t,i}^{\text{prox}} = \arg \min_{\delta \in \mathbb{R}^n} \left\{ \frac{1}{2} \|\delta\|_2^2 + \lambda \|\Pi^\top \delta - \Delta z_{t,i}\|_2^2 \right\}.$$

With $M = \Pi^\top \Pi$, the closed-form solution and lifted protected update are

$$u_{t,i}^{\text{prox}} = (I + 2\lambda M)^{-1} (2\lambda \Delta z_{t,i}), \quad \delta_{t,i}^{\text{prox}} = \Pi u_{t,i}^{\text{prox}}, \quad \hat{O}_{t,i} = O_{t,i}^{(s)} + \delta_{t,i}^{\text{prox}}.$$

Stacking all rows gives $\hat{O}_t \in \mathbb{R}^{m \times n}$. The parameter update is

$$\theta_t = (1 - \eta \text{wd}) \theta_{t-1} - \eta \gamma_t \hat{O}_t, \quad \gamma_t = \sigma \frac{\sqrt{mn}}{\|\hat{O}_t\|_F + \varepsilon},$$

where wd is the weight decay coefficient, $\varepsilon = 10^{-8}$, and γ_t follows the scaling of Si et al. [39]. Overall, FOGO combines dual-stream orthogonalized updates with multiscale directional memory: geodesic fusion preserves plasticity, the online codebook filters short-term interference, and frozen centroids impose stricter long-term protection. The proximal step maps these corrections back to parameter space with controlled distortion.

4.4 Theoretical Analysis

Theorem 4 (Memory protection preserves learned directions). This result is stated in the projected update space \mathbb{R}^d , before the proximal lifting step. Consider a projected update $x_{t,i} \in \mathbb{R}^d$. Let $\mathcal{I}_{t,i}^{\text{mem}}$ be an active memory index set, where each $a \in \mathcal{I}_{t,i}^{\text{mem}}$ corresponds to a normalized direction $c_a \in \mathbb{R}^d$ and a nonnegative weight $\nu_a \geq 0$. Define

$$\Omega_{t,i}^{\text{mem}} = \sum_{a \in \mathcal{I}_{t,i}^{\text{mem}}} \nu_a c_a c_a^\top.$$

The memory-protected update is $x_{t,i}^+ = (I - \gamma_{\text{mem}} \Omega_{t,i}^{\text{mem}}) x_{t,i}$. If $\Omega_{t,i}^{\text{mem}} \neq 0$ and

$$0 \leq \gamma_{\text{mem}} \leq \frac{1}{\lambda_{\max}(\Omega_{t,i}^{\text{mem}})},$$

then

$$\|(\Omega_{t,i}^{\text{mem}})^{1/2} x_{t,i}^+\|_2 \leq \|(\Omega_{t,i}^{\text{mem}})^{1/2} x_{t,i}\|_2.$$

Moreover, for any $v \in \text{Null}(\Omega_{t,i}^{\text{mem}})$,

$$(I - \gamma_{\text{mem}} \Omega_{t,i}^{\text{mem}}) v = v.$$

Thus, memory protection reduces update energy along active learned directions while leaving unconstrained directions unchanged.

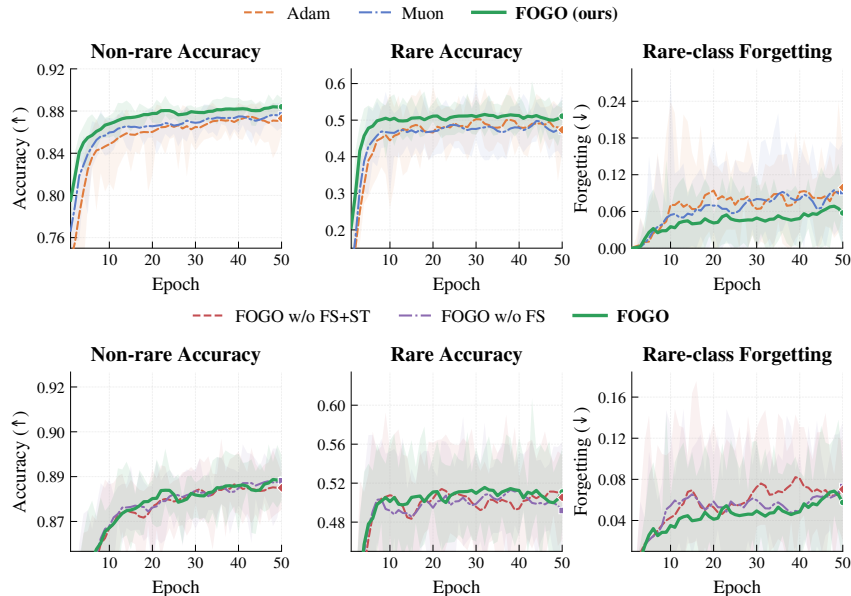


Figure 2: **Class-imbalanced CIFAR-10. Top:** FOGO outperforms Adam and Muon under class-imbalanced training, improving rare-class accuracy and reducing rare-class forgetting while preserving non-rare accuracy. **Bottom:** Removing slow-fast fusion (w/o FS) and short-term filtering (w/o FS+ST) progressively increases rare-class forgetting. Curves show the mean over ten seeds, with shaded regions denoting one standard deviation.

5 Experiments

5.1 Class-Imbalanced Learning

Setup. We introduce a controlled class-imbalanced CIFAR-10 benchmark to probe *short-term forgetting*. ResNet-18 [17] is trained from scratch for 50 epochs, with five *rare* classes retaining only 10% of their training samples. This creates sparse rare-class gradients that are persistently dominated by majority-class updates. We report rare- and non-rare-class accuracy separately on the standard test set, measuring rare-class forgetting as the best-so-far accuracy drop. Details are in Appendix D.

Results and Ablation. As shown in Fig. 2, FOGO improves both rare- and non-rare-class accuracy over Adam and Muon by roughly 2–3 percentage points while reducing rare-class forgetting by about 6 points, indicating that its correction preserves low-frequency learning signals without trading off frequent-class performance. The ablation shows that removing fast-slow fusion causes mild degradation, whereas removing both fusion and short-term filtering substantially increases forgetting—confirming short-term filtering as the primary contributor, with fusion providing additional gain. Appendix F.2 shows that FOGO also achieves smoother and faster convergence.

5.2 Continual Visual Learning

Setup. We evaluate FOGO on continual visual learning in two regimes. In *domain-incremental learning (Domain-IL)*, we use PACS [29], where seven classes appear sequentially across four domains (Photo, Art Painting, Cartoon, Sketch). We train an ImageNet-pretrained ResNet-18 with fixed batch-normalization statistics and test FOGO both without replay and with ER [6], comparing against plasticity-oriented optimizers including CBP [8] and FIRE [16]. In *class-incremental learning (Class-IL)*, we split CIFAR-10 into five tasks and train ResNet-18 from scratch using DER++ [4], replacing its optimizer with FOGO to test whether direction-aware updates improve retention beyond replay. We compare against Adam, Muon, and UPGD [10] under the same 20-epoch budget. Details, extended results, and ablations are in Appendices D, E, and F.

Table 1: **Domain-incremental learning on PACS**. Results averaged over three domain orders and two seeds. AP: Average Performance; AF: Average Forgetting. Best in bold, second-best underlined. Time in minutes.

Regime	CL Method	Optimizer	Memory	Mem. (MB) ↓	Time (m) ↓	AP (%) ↑	AF (%) ↓
Free	None	Adam	None	< 0.1	7.49	83.34 ± 1.65	15.45 ± 3.85
Free	None	Muon	None	< 0.1	<u>8.15</u>	<u>87.81 ± 1.70</u>	<u>9.44 ± 3.07</u>
Free	None	CBP	None	< 0.1	12.10	82.78 ± 1.96	15.94 ± 4.18
Free	None	FIRE	None	< 0.1	11.14	75.94 ± 2.34	20.98 ± 5.54
Free	None	FOGO	Centroids	<u>0.55</u>	<u>9.84</u>	87.89 ± 2.94	6.77 ± 2.31
Replay	ER	Adam	Buffer	57.4	8.21	87.50 ± 1.06	9.81 ± 1.62
Replay	ER	Muon	Buffer	57.4	<u>8.88</u>	<u>89.20 ± 1.91</u>	<u>7.56 ± 0.90</u>
Replay	ER	CBP	Buffer	57.4	13.60	84.77 ± 4.05	13.01 ± 5.70
Replay	ER	FIRE	Buffer	57.4	11.52	82.79 ± 2.31	13.36 ± 0.97
Replay	ER	FOGO	Buffer + Centroids	<u>58.0</u>	<u>10.44</u>	90.24 ± 3.13	4.21 ± 0.85

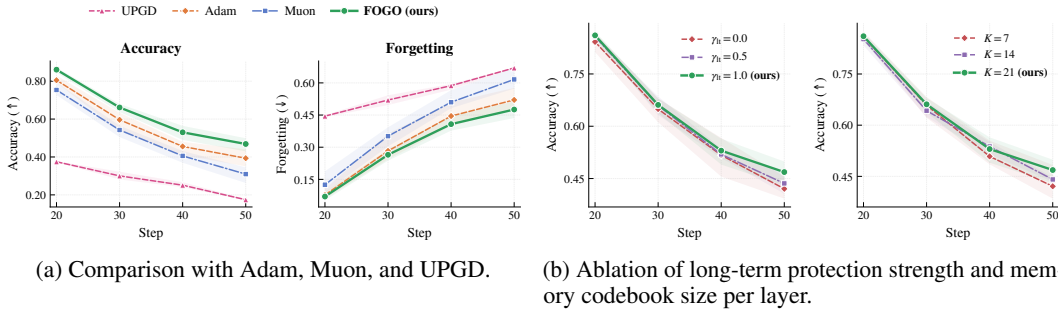


Figure 3: **Class-incremental learning on CIFAR-10**. Left: comparison with Adam, Muon, and UPGD. Right: ablations on long-term protection strength γ_{lt} and the number of frozen centroids per layer. Results are averaged over five random seeds.

Results & Ablation Study. Table 1 shows that FOGO consistently improves retention in Domain-IL. Without replay, FOGO achieves the lowest AF, reducing forgetting by 2.67 points over Muon while matching its AP, and improving AP by 4.55 points over Adam. With ER, FOGO further improves ER+Adam by 2.74 AP points and 5.60 AF points. Notably, replay-free FOGO also *surpasses ER+Adam in both AP and AF using only 0.55MB of centroid memory versus 57.4MB for replay*, with only a modest time increase. CBP and FIRE perform worse, indicating that plasticity alone is insufficient for stable domain-incremental learning.

Fig. 3 shows that FOGO improves Class-IL performance over Adam, Muon, and UPGD, achieving higher accuracy while reducing forgetting. Although Muon orthogonalizes updates, it lacks an explicit memory of task-relevant directions; UPGD estimates utility from the current task, which can leave earlier class-specific directions insufficiently protected. The ablations further show that increasing the long-term protection strength γ_{lt} and the number of frozen centroids consistently improves retention. These trends support our central claim: orthogonalized updates help balance directions, while explicit directional memory is needed to preserve knowledge across tasks.

5.3 Continual Fine-tuning

Setup. We evaluate continual multimodal fine-tuning on Continual VisualQA, a VQA v2 [14]-based benchmark with 200K images and 1.1M questions. Following CL-MoE [21], the benchmark is divided into 10 reasoning-type tasks: recognition, location, judgment, commonsense, counting, action, color, type, subcategory, and causal reasoning. We fine-tune LLaVA-1.5-7B [30] with the LoRAMoE [9] architecture and vary only the optimizer among AdamW, Muon, and FOGO, thereby isolating the effect of the update rule under the same parameter-efficient MoE setting. We report Average Performance (AP) and Sum Forgetting (SF) across all tasks. We compare against CL-MoE,

Table 2: **Continual learning results on VQA v2.** We compare CL-MoE and LoRAMoE with AdamW, Muon, and FOGO. AP denotes Average Performance, and SF denotes Sum Forgetting. Best results are bolded and second-best underlined.

Method	VQA v2 Task Types										AP \uparrow	SF \downarrow
	Rec.	Loc.	Jud.	Com.	Cou.	Act.	Col.	Typ.	Sub.	Cau.		
CL-MoE	55.74	41.74	80.39	<u>76.77</u>	<u>49.47</u>	75.41	73.56	63.17	61.03	30.41	60.77	17.70
LoRAMoE + AdamW	<u>55.88</u>	41.45	<u>80.64</u>	76.45	48.90	75.48	73.36	62.68	<u>61.97</u>	<u>29.95</u>	60.68	18.12
LoRAMoE + Muon	57.72	41.31	80.48	<u>76.77</u>	48.88	<u>76.04</u>	<u>73.73</u>	<u>63.25</u>	61.35	29.03	<u>60.86</u>	<u>17.39</u>
LoRAMoE + FOGO	57.72	<u>41.60</u>	82.95	79.95	52.91	77.83	75.56	63.91	62.72	29.85	62.50	7.14

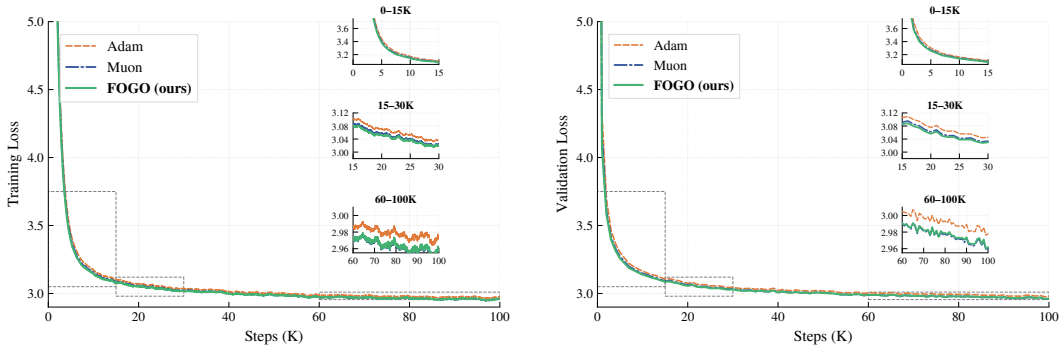


Figure 4: Training loss (left) and validation loss (right) during GPT-2 pretraining.

since conventional continual-learning baselines were reported to perform substantially worse in [21]. Further details are provided in Appendix D.

Results. Table 2 shows that FOGO consistently outperforms AdamW, Muon, and the strong CL-MoE baseline, improving average accuracy by about 2 points and reducing total forgetting by roughly 10 points over the ten tasks. These gains suggest that FOGO better preserves important LoRA expert update directions through its compact centroid memory. Appendix F provides further analysis of training behavior, efficiency, and expert plasticity, showing that FOGO induces more balanced expert feature variance and helps mitigate expert collapse and destructive updates during continual learning.

5.4 Language Pretraining

Setup. We evaluate language-model pretraining from scratch on OpenWebText [13] using GPT-2 Small (125M) [34] implemented in nanoGPT [25]. All methods are trained for 100K steps, corresponding to approximately 49.2B tokens, with the same architecture, data order, token budget, context length of 1024, and learning-rate schedule. We compare FOGO with Adam and Muon. Following the standard Muon hybrid setup, Muon and FOGO are applied to matrix-valued parameters, while Adam updates the remaining parameters. We report training and validation loss over tokens to assess optimization efficiency and language-modeling performance.

Results. Fig. 4 shows that FOGO also performs well in standard unsupervised learning via the popular next-token-prediction scheme. Specifically, FOGO converges faster than both Adam and Muon during GPT-2 pretraining: the zoomed-in panels reveal a clear gap in validation loss throughout the first 30K steps, after which all three optimizers gradually approach a similar final loss. This suggests that FOGO’s mechanism is beneficial not only in the continual-learning setting but also in conventional large-scale language model training.

6 Conclusion

We proposed FOGO, a scalable optimizer that unifies standard and continual learning under a single interference-resolution framework. By combining spectral orthogonalization with a compact

random-projection codebook, FOGO detects and corrects gradient interference at every step without storing raw data. Across class-imbalanced learning, continual visual learning, LLaVA-7B fine-tuning, and GPT-2 pretraining, FOGO consistently improves convergence, performance, and retention over Adam and Muon. Forgetting remains an open challenge, but our results suggest that resolving it at the optimizer level is both practical and effective. Natural extensions include dynamic codebook sizing, boundary-free continual learning, and adaptive centroid management—steps toward a self-organizing directional memory for lifelong learning.

Acknowledgements

This work was supported by the US Army International Technology Center Pacific (ITC-IPAC) under Contract No. FA520923C0020. The authors acknowledge the National Computational Infrastructure (NCI Australia), an NCRIS-enabled capability supported by the Australian Government, for providing computational resources used in this study. We also acknowledge the Katana computational cluster, supported by Research Technology Services at UNSW Sydney.

References

- [1] David Abel, Andre Barreto, Benjamin Van Roy, Doina Precup, Hado van Hasselt, and Satinder Singh. A definition of continual reinforcement learning. In *NeurIPS*, 2023.
- [2] Ali Behrouz, Meisam Razaviyayn, Peilin Zhong, and Vahab Mirrokni. Nested learning: The illusion of deep learning architectures. In *NeurIPS*, 2025.
- [3] Jeremy Bernstein and Laker Newhouse. Old optimizer, new norm: An anthology. *arXiv preprint arXiv:2409.20325*, 2024.
- [4] Pietro Buzzega, Matteo Boschini, Angelo Porrello, Davide Abati, and Simone Calderara. Dark experience for general continual learning: a strong, simple baseline. *NeurIPS*, 33:15920–15930, 2020.
- [5] Arslan Chaudhry, Marc’Aurelio Ranzato, Marcus Rohrbach, and Mohamed Elhoseiny. Efficient lifelong learning with a-GEM. In *ICLR*, 2019.
- [6] Arslan Chaudhry, Marcus Rohrbach, Mohamed Elhoseiny, Thalaiyasingam Ajanthan, Puneet K Dokania, Philip HS Torr, and Marc’Aurelio Ranzato. On tiny episodic memories in continual learning. *arXiv preprint arXiv:1902.10486*, 2019.
- [7] Matthias De Lange, Rahaf Aljundi, Marc Masana, Sarah Parisot, Xu Jia, Aleš Leonardis, Gregory Slabaugh, and Tinne Tuytelaars. A continual learning survey: Defying forgetting in classification tasks. *IEEE transactions on pattern analysis and machine intelligence*, 44(7):3366–3385, 2021.
- [8] Shibhansh Dohare, J Fernando Hernandez-Garcia, Qingfeng Lan, Parash Rahman, A Rupam Mahmood, and Richard S Sutton. Loss of plasticity in deep continual learning. *Nature*, 632(8026):768–774, 2024.
- [9] Shihan Dou, Enyu Zhou, Yan Liu, Songyang Gao, Jun Zhao, Wei Shen, Yuhao Zhou, Zhiheng Xi, Xiao Wang, Xiaoran Fan, Shiliang Pu, Jiang Zhu, Rui Zheng, Tao Gui, Qi Zhang, and Xuanjing Huang. Loramoe: Revolutionizing mixture of experts for maintaining world knowledge in language model alignment, 2023.
- [10] Mohamed Elsayed and A. Rupam Mahmood. Addressing loss of plasticity and catastrophic forgetting in continual learning. In *ICLR*, 2024.
- [11] Mehrdad Farajtabar, Navid Azizan, Alex Mott, and Ang Li. Orthogonal gradient descent for continual learning. In *AISTATS*, pages 3762–3773. PMLR, 2020.
- [12] Dan Friedman and Adji Bousso Dieng. The vendi score: A diversity evaluation metric for machine learning. *TMLR*, 2023. ISSN 2835-8856.
- [13] Aaron Gokaslan and Vanya Cohen. Openwebtext corpus. <http://Skylion007.github.io/OpenWebTextCorpus>, 2019.
- [14] Yash Goyal, Tejas Khot, Douglas Summers-Stay, Dhruv Batra, and Devi Parikh. Making the v in vqa matter: Elevating the role of image understanding in visual question answering. In *CVPR*, pages 6904–6913, 2017.
- [15] Vineet Gupta, Tomer Koren, and Yoram Singer. Shampoo: Preconditioned stochastic tensor optimization. In *ICML*, pages 1842–1850. PMLR, 2018.

- [16] Isaac Han, Sangyeon Park, Seungwon Oh, Donghu Kim, Hojoon Lee, and Kyung-Joong Kim. Fire: Frobenius-isometry reinitialization for balancing the stability-plasticity tradeoff. *ICLR*, 2026.
- [17] Kaiming He, Xiangyu Zhang, Shaoqing Ren, and Jian Sun. Deep residual learning for image recognition. In *CVPR*, pages 770–778, 2016.
- [18] Nicholas J Higham. *Functions of matrices: theory and computation*. SIAM, 2008.
- [19] Edward J Hu, yelong shen, Phillip Wallis, Zeyuan Allen-Zhu, Yuanzhi Li, Shean Wang, Lu Wang, and Weizhu Chen. LoRA: Low-rank adaptation of large language models. In *ICLR*, 2022.
- [20] Shengding Hu, Yuge Tu, Xu Han, Ganqu Cui, Chaoqun He, Weilin Zhao, Xiang Long, Zhi Zheng, Yewei Fang, Yuxiang Huang, Xinrong Zhang, Zhen Leng Thai, Chongyi Wang, Yuan Yao, Chenyang Zhao, Jie Zhou, Jie Cai, Zhongwu Zhai, Ning Ding, Chao Jia, Guoyang Zeng, dahai li, Zhiyuan Liu, and Maosong Sun. MiniCPM: Unveiling the potential of small language models with scalable training strategies. In *COLM*, 2024.
- [21] Tianyu Huai, Jie Zhou, Xingjiao Wu, Qin Chen, Qingchun Bai, Ze Zhou, and Liang He. Cl-moe: Enhancing multimodal large language model with dual momentum mixture-of-experts for continual visual question answering. In *CVPR*, pages 19608–19617, 2025.
- [22] William B Johnson, Joram Lindenstrauss, et al. Extensions of lipschitz mappings into a hilbert space. *Contemporary mathematics*, 26(189-206):1, 1984.
- [23] Keller Jordan, Yuchen Jin, Vlado Boza, Jiacheng You, Franz Cesista, Laker Newhouse, and Jeremy Bernstein. Muon: An optimizer for hidden layers in neural networks, 2024. URL <https://kellerjordan.github.io/posts/muon/>.
- [24] Jaehun Jung, Seungju Han, Ximing Lu, Skyler Hallinan, David Acuna, Shrimai Prabhumoye, Mostofa Patwary, Mohammad Shoeybi, Bryan Catanzaro, and Yejin Choi. Prismatic synthesis: Gradient-based data diversification boosts generalization in LLM reasoning. In *NeurIPS*, 2025.
- [25] Andrej Karpathy. Nanogpt. <https://github.com/karpathy/nanoGPT>, 2022.
- [26] Diederik P Kingma and Jimmy Ba. Adam: A method for stochastic optimization. *arXiv preprint arXiv:1412.6980*, 2014.
- [27] James Kirkpatrick, Razvan Pascanu, Neil Rabinowitz, Joel Veness, Guillaume Desjardins, Andrei A Rusu, Kieran Milan, John Quan, Tiago Ramalho, Agnieszka Grabska-Barwinska, et al. Overcoming catastrophic forgetting in neural networks. *Proceedings of the national academy of sciences*, 114(13):3521–3526, 2017.
- [28] Alex Krizhevsky. Learning multiple layers of features from tiny images. Technical report, University of Toronto, 2009.
- [29] Da Li, Yongxin Yang, Yi-Zhe Song, and Timothy M Hospedales. Deeper, broader and artier domain generalization. In *ICCV*, pages 5542–5550, 2017.
- [30] Haotian Liu, Chunyuan Li, Qingyang Wu, and Yong Jae Lee. Visual instruction tuning. *NeurIPS*, 36: 34892–34916, 2023.
- [31] Jingyuan Liu, Jianlin Su, Xingcheng Yao, Zhejun Jiang, Guokun Lai, Yulun Du, Yidao Qin, Weixin Xu, Enzhe Lu, Junjie Yan, et al. Muon is scalable for llm training. *arXiv preprint arXiv:2502.16982*, 2025.
- [32] David Lopez-Paz and Marc’Aurelio Ranzato. Gradient episodic memory for continual learning. *NIPS*, 30, 2017.
- [33] Ilya Loshchilov and Frank Hutter. Decoupled weight decay regularization. In *ICLR*, 2019. URL <https://openreview.net/forum?id=Bkg6RiCqY7>.
- [34] Alec Radford, Jeffrey Wu, Rewon Child, David Luan, Dario Amodei, Ilya Sutskever, et al. Language models are unsupervised multitask learners. *OpenAI blog*, 1(8):9, 2019.
- [35] Matthew Riemer, Ignacio Cases, Robert Ajemian, Miao Liu, Irina Rish, Yuhai Tu, and Gerald Tesauero. Learning to learn without forgetting by maximizing transfer and minimizing interference. In *ICLR*, 2019.
- [36] Andrei A Rusu, Neil C Rabinowitz, Guillaume Desjardins, Hubert Soyer, James Kirkpatrick, Koray Kavukcuoglu, Razvan Pascanu, and Raia Hadsell. Progressive neural networks. *arXiv preprint arXiv:1606.04671*, 2016.

- [37] Gobinda Saha, Isha Garg, and Kaushik Roy. Gradient projection memory for continual learning. In *ICLR*, 2021.
- [38] Wei Shen, Ruichuan Huang, Minhui Huang, Cong Shen, and Jiawei Zhang. On the convergence analysis of muon. *arXiv preprint arXiv:2505.23737*, 2025.
- [39] Chongjie Si, Debing Zhang, and Wei Shen. Adamuon: Adaptive muon optimizer. *arXiv preprint arXiv:2507.11005*, 2025.
- [40] Jianlin Su, Murtadha Ahmed, Yu Lu, Shengfeng Pan, Wen Bo, and Yunfeng Liu. Roformer: Enhanced transformer with rotary position embedding. *Neurocomputing*, 568:127063, 2024.
- [41] Hugo Touvron, Thibaut Lavril, Gautier Izacard, Xavier Martinet, Marie-Anne Lachaux, Timothée Lacroix, Baptiste Rozière, Naman Goyal, Eric Hambro, Faisal Azhar, et al. Llama: Open and efficient foundation language models. *arXiv preprint arXiv:2302.13971*, 2023.
- [42] Liyuan Wang, Xingxing Zhang, Hang Su, and Jun Zhu. A comprehensive survey of continual learning: Theory, method and application. *IEEE transactions on pattern analysis and machine intelligence*, 46(8): 5362–5383, 2024.
- [43] Xiao Wang, Tianze Chen, Qiming Ge, Han Xia, Rong Bao, Rui Zheng, Qi Zhang, Tao Gui, and Xuan-Jing Huang. Orthogonal subspace learning for language model continual learning. In *Findings of EMNLP*, pages 10658–10671, 2023.

A Extended Background

Orthogonalization. Let $B_t \in \mathbb{R}^{m \times n}$ with compact SVD $B_t = U_t \Sigma_t V_t^\top$, where $\Sigma_t = \text{diag}(\sigma_1, \dots, \sigma_r)$ and $\sigma_1 \geq \dots \geq \sigma_r > 0$. The orthogonalized update $\mathcal{O}(B_t) := U_t V_t^\top$ discards Σ_t while retaining the left and right singular directions. Intuitively, this equalizes the influence of all singular modes: rather than allowing a few high-energy directions to dominate the step, orthogonalization reweights the update toward under-represented directions. Bernstein and Newhouse [3] formalize this by showing that Muon and related optimizers perform steepest descent under a spectral-norm constraint.

Newton–Schulz iterations. The polar factor $\mathcal{O}(B_t)$ is approximated without a full SVD via the Newton–Schulz iteration. Starting from $X_0 = B_t / \|B_t\|_F$, the recurrence $X_{k+1} = \frac{1}{2} X_k (3I - X_k^\top X_k)$ converges quadratically to $U_t V_t^\top$ when $\|B_t\|_2 < 1$. In practice, $T = 5$ iterations suffice [23].

G-Vendi Score. G-Vendi Score [24] extends the Vendi score [12] from sample embeddings to the gradient space of deep networks. For each sample i , the per-sample gradient $G_i = \nabla_\theta \mathcal{L}(\theta; x_i, y_i) \in \mathbb{R}^{|\theta|}$ is projected via $G_i^{\text{proj}} = \Pi^\top G_i$. The G-Vendi Score is computed from the Gram matrix $K \in \mathbb{R}^{N \times N}$ of projected gradients, where K_{ij} denotes the normalized similarity between G_i^{proj} and G_j^{proj} . This provides a model-centric embedding whose clustering structure reveals representative update directions and the geometry of the gradient distribution.

B Theoretical Results

B.1 Proof of Theorem 1

Recall that $\mathcal{P}_t^{(r)}(X) = U_t^{(r)} U_t^{(r)\top} X V_t^{(r)} V_t^{(r)\top}$ and $\mathcal{P}_t^{(r)\perp}(X) = X - \mathcal{P}_t^{(r)}(X)$, so both $\mathcal{P}_t^{(r)}$ and $\mathcal{P}_t^{(r)\perp}$ are linear operators on $\mathbb{R}^{m \times n}$. Under the momentum update $B_t = \mu B_{t-1} + G_t$, we have

$$R_t = \|\mathcal{P}_t^{(r)\perp}(B_t)\|_F = \|\mathcal{P}_t^{(r)\perp}(\mu B_{t-1} + G_t)\|_F. \quad (4)$$

By linearity of $\mathcal{P}_t^{(r)\perp}$ and the triangle inequality,

$$R_t \leq \mu \|\mathcal{P}_t^{(r)\perp}(B_{t-1})\|_F + \|\mathcal{P}_t^{(r)\perp}(G_t)\|_F = \mu \|\mathcal{P}_t^{(r)\perp}(B_{t-1})\|_F + \varepsilon_t. \quad (5)$$

It remains to bound $\|\mathcal{P}_t^{(r)\perp}(B_{t-1})\|_F$. By definition,

$$\mathcal{P}_t^{(r)\perp}(B_{t-1}) = (I - \mathcal{P}_t^{(r)})(B_{t-1}). \quad (6)$$

Adding and subtracting $\mathcal{P}_{t-1}^{(r)}(B_{t-1})$ gives

$$(I - \mathcal{P}_t^{(r)})(B_{t-1}) = (I - \mathcal{P}_{t-1}^{(r)})(B_{t-1}) + (\mathcal{P}_{t-1}^{(r)} - \mathcal{P}_t^{(r)})(B_{t-1}). \quad (7)$$

Taking Frobenius norms and applying the triangle inequality yields

$$\|\mathcal{P}_t^{(r)\perp}(B_{t-1})\|_F \leq \|(I - \mathcal{P}_{t-1}^{(r)})(B_{t-1})\|_F + \|(\mathcal{P}_{t-1}^{(r)} - \mathcal{P}_t^{(r)})(B_{t-1})\|_F. \quad (8)$$

Since

$$\|(I - \mathcal{P}_{t-1}^{(r)})(B_{t-1})\|_F = R_{t-1},$$

we obtain

$$\|\mathcal{P}_t^{(r)\perp}(B_{t-1})\|_F \leq R_{t-1} + \|(\mathcal{P}_{t-1}^{(r)} - \mathcal{P}_t^{(r)})(B_{t-1})\|_F. \quad (9)$$

By the slow-drift assumption,

$$\|\mathcal{P}_t^{(r)} - \mathcal{P}_{t-1}^{(r)}\|_{F \rightarrow F} \leq \delta_t,$$

hence

$$\|(\mathcal{P}_{t-1}^{(r)} - \mathcal{P}_t^{(r)})(B_{t-1})\|_F \leq \delta_t \|B_{t-1}\|_F. \quad (10)$$

Therefore,

$$\|\mathcal{P}_t^{(r)\perp}(B_{t-1})\|_F \leq R_{t-1} + \delta_t \|B_{t-1}\|_F. \quad (11)$$

Substituting this bound into the earlier inequality gives

$$R_t \leq \mu R_{t-1} + \mu \delta_t \|B_{t-1}\|_F + \varepsilon_t, \quad (12)$$

which proves the claim. \square

B.2 Proof of Corollary 5

Corollary 5 (Unrolled suppression bound). Under the assumptions of Theorem 1, let

$$a_t := \mu \delta_t \|B_{t-1}\|_F + \varepsilon_t.$$

Then the off-subspace residual satisfies

$$R_t \leq \mu^t R_0 + \sum_{k=1}^t \mu^{t-k} a_k. \quad (13)$$

In particular, if $a_t \leq \bar{a}$ for all t , then

$$R_t \leq \mu^t R_0 + \bar{a} \frac{1 - \mu^t}{1 - \mu}, \quad (14)$$

and hence

$$\limsup_{t \rightarrow \infty} R_t \leq \frac{\bar{a}}{1 - \mu}. \quad (15)$$

Therefore, the off-subspace residual contracts geometrically up to a steady-state floor of order $\bar{a}/(1 - \mu)$. In particular, if $a_t \rightarrow 0$, then $R_t \rightarrow 0$.

Proof of Corollary 5. From Theorem 1,

$$R_t \leq \mu R_{t-1} + \mu \delta_t \|B_{t-1}\|_F + \varepsilon_t = \mu R_{t-1} + a_t. \quad (16)$$

Iterating this recursion yields

$$R_t \leq \mu^t R_0 + \sum_{k=1}^t \mu^{t-k} a_k. \quad (17)$$

This proves the first claim. If $a_t \leq \bar{a}$ for all t , then

$$R_t \leq \mu^t R_0 + \bar{a} \sum_{k=1}^t \mu^{t-k} = \mu^t R_0 + \bar{a} \frac{1 - \mu^t}{1 - \mu}. \quad (18)$$

Since $0 \leq \mu < 1$, taking $t \rightarrow \infty$ gives

$$\limsup_{t \rightarrow \infty} R_t \leq \frac{\bar{a}}{1 - \mu}. \quad (19)$$

Thus, R_t contracts geometrically up to a steady-state floor of order $\bar{a}/(1 - \mu)$.

Finally, if $a_t \rightarrow 0$, then for any $\epsilon > 0$ there exists T such that $a_k \leq \epsilon$ for all $k \geq T$. Splitting the sum at T ,

$$\sum_{k=1}^t \mu^{t-k} a_k = \sum_{k=1}^{T-1} \mu^{t-k} a_k + \sum_{k=T}^t \mu^{t-k} a_k. \quad (20)$$

The first term tends to 0 as $t \rightarrow \infty$, because T is fixed and thus it contains only finitely many terms $\mu^{t-k} a_k$, each converging to 0. For the second term,

$$\sum_{k=T}^t \mu^{t-k} a_k \leq \epsilon \sum_{k=T}^t \mu^{t-k} \leq \frac{\epsilon}{1 - \mu}. \quad (21)$$

Hence

$$\limsup_{t \rightarrow \infty} \sum_{k=1}^t \mu^{t-k} a_k \leq \frac{\epsilon}{1 - \mu}.$$

Since this is true for every $\epsilon > 0$, the limsup is at most 0. As the sum is nonnegative for all t , its liminf is at least 0. Therefore,

$$\sum_{k=1}^t \mu^{t-k} a_k \rightarrow 0.$$

Together with $\mu^t R_0 \rightarrow 0$, this implies $R_t \rightarrow 0$. \square

This shows that off-subspace directions are suppressed unless they are continually replenished by new gradient energy or sustained by persistent subspace drift.

B.3 Spectral Equalization by Orthogonalization

Proposition 6 (Orthogonalization as Spectral equalization). Let $B = U\Sigma V^\top \in \mathbb{R}^{m \times n}$ have rank k , with singular values $\sigma_1 \geq \dots \geq \sigma_k > 0$, and let $O = UV^\top$ be its orthogonalized update. For each singular mode $E_i = u_i v_i^\top$,

$$\langle B, E_i \rangle_F = \sigma_i, \quad \langle O, E_i \rangle_F = 1.$$

Hence, for any $i, j \leq k$,

$$\frac{\langle B, E_i \rangle_F}{\langle B, E_j \rangle_F} = \frac{\sigma_i}{\sigma_j}, \quad \frac{\langle O, E_i \rangle_F}{\langle O, E_j \rangle_F} = 1.$$

Thus, orthogonalization preserves the singular directions of B while equalising their coefficients. In particular, a weak mode E_i receives a relative amplification factor σ_j/σ_i compared with any stronger mode E_j .

Proof of Proposition 6 Since

$$B = \sum_{i=1}^k \sigma_i u_i v_i^\top, \quad O = UV^\top = \sum_{i=1}^k u_i v_i^\top,$$

each singular mode $E_i = u_i v_i^\top$ appears in B with coefficient σ_i , and in O with coefficient 1. Moreover, the rank-one matrices $\{E_i\}_{i=1}^k$ are orthonormal under the Frobenius inner product:

$$\langle E_i, E_j \rangle_F = \text{tr}(v_i u_i^\top u_j v_j^\top) = (u_i^\top u_j)(v_i^\top v_j) = \delta\{i = j\}.$$

Therefore,

$$\langle B, E_i \rangle_F = \sigma_i, \quad \langle O, E_i \rangle_F = 1,$$

The ratio statements follow directly. Intuitively, orthogonalization equalizes all retained singular modes, allowing weak but useful directions to remain visible rather than being overwhelmed by dominant modes.

B.4 Gradient Geometry Preservation under Random Projection

We justify operating on projected gradients rather than full high-dimensional gradients. Let $\mathcal{G} = \{G_i\}_{i=1}^N \subset \mathbb{R}^{|\theta|}$ be a finite set of gradient vectors, and let $\Pi \in \mathbb{R}^{|\theta| \times d}$ be a Rademacher random projection with entries scaled by $1/\sqrt{d}$. By the Johnson–Lindenstrauss lemma, for any $\epsilon \in (0, 1)$, if $d = \mathcal{O}(\epsilon^{-2} \log N)$, then with high probability, for all i, j ,

$$(1 - \epsilon) \|G_i - G_j\|_2^2 \leq \|\Pi^\top G_i - \Pi^\top G_j\|_2^2 \leq (1 + \epsilon) \|G_i - G_j\|_2^2.$$

Thus, projected gradients preserve pairwise geometry up to small multiplicative distortion. This supports clustering and conflict detection in the projected space, while reducing memory and computation from $|\theta|$ dimensions to d dimensions. For example, even for a model with $|\theta| = 100\text{M}$ parameters, the required projected dimension depends logarithmically on the number of tracked gradients N , not on $|\theta|$; in practice, dimensions such as $d = 256$ or 512 already provide a compact surrogate for online directional memory.

Proof Sketch. The result follows directly from the Johnson–Lindenstrauss lemma [22] applied to the finite set \mathcal{G} . A Rademacher matrix with $1/\sqrt{d}$ scaling is a sub-Gaussian Johnson–Lindenstrauss transform. Hence, for any fixed pair (G_i, G_j) , the projected squared distance $\|\Pi^\top (G_i - G_j)\|_2^2$ concentrates around $\|G_i - G_j\|_2^2$ within a factor $1 \pm \epsilon$. A union bound over all $N(N-1)/2$ distinct pairs gives the stated guarantee when $d = \mathcal{O}(\epsilon^{-2} \log N)$.

B.5 Derivation of the Proximal Lifting Solution

We derive the closed-form solution used to lift projected corrections back to the original update space. Recall that $\Pi \in \mathbb{R}^{n \times d}$ is the fixed random projection, $P_{t,i}^{(s)} = O_{t,i}^{(s)} \Pi \in \mathbb{R}^d$ is the projected slow-stream update, and $\bar{z}_{t,i} \in \mathbb{R}^d$ is the memory-protected direction after short- and long-term filtering. The projected correction is

$$\Delta z_{t,i} = \bar{z}_{t,i} - P_{t,i}^{(s)} \in \mathbb{R}^d.$$

Since Π is not invertible, we find the smallest correction $\delta_{t,i} \in \mathbb{R}^n$ whose projection matches $\Delta z_{t,i}$ in a least-squares sense:

$$\delta_{t,i}^{\text{prox}} = \arg \min_{\delta \in \mathbb{R}^n} \left\{ \frac{1}{2} \|\delta\|_2^2 + \lambda \|\delta^\top \Pi - \Delta z_{t,i}\|_2^2 \right\}.$$

Let

$$f(\delta) = \frac{1}{2} \|\delta\|_2^2 + \lambda \|\Pi^\top \delta - \Delta z_{t,i}\|_2^2.$$

Taking the gradient gives

$$\nabla_\delta f = \delta + 2\lambda \Pi (\Pi^\top \delta - \Delta z_{t,i}).$$

Setting $\nabla_\delta f = 0$ yields

$$(I + 2\lambda \Pi \Pi^\top) \delta = 2\lambda \Pi \Delta z_{t,i},$$

and hence the direct high-dimensional solution is

$$\delta_{t,i}^{\text{prox}} = (I + 2\lambda \Pi \Pi^\top)^{-1} (2\lambda \Pi \Delta z_{t,i}).$$

Using the identity

$$(I + 2\lambda \Pi \Pi^\top)^{-1} \Pi = \Pi (I + 2\lambda \Pi^\top \Pi)^{-1},$$

we obtain the equivalent low-dimensional form

$$\delta_{t,i}^{\text{prox}} = \Pi (I + 2\lambda \Pi^\top \Pi)^{-1} (2\lambda \Delta z_{t,i}).$$

Therefore, with $M = \Pi^\top \Pi$, we compute

$$u_{t,i}^{\text{prox}} = (I + 2\lambda M)^{-1} (2\lambda \Delta z_{t,i}), \quad \delta_{t,i}^{\text{prox}} = \Pi u_{t,i}^{\text{prox}}.$$

The objective is strongly convex for $\lambda > 0$, so the minimizer is unique.

B.6 Proof of Theorem 4

For any $a \in \mathcal{I}_{t,i}^{\text{mem}}$, the rank-one matrix $c_a c_a^\top$ is symmetric positive semidefinite. Since $\nu_a \geq 0$, the memory operator

$$\Omega_{t,i}^{\text{mem}} = \sum_{a \in \mathcal{I}_{t,i}^{\text{mem}}} \nu_a c_a c_a^\top$$

is also symmetric positive semidefinite. If $\Omega_{t,i}^{\text{mem}} = 0$, then $x_{t,i}^+ = x_{t,i}$, and both claims hold trivially. We therefore consider $\Omega_{t,i}^{\text{mem}} \neq 0$.

Since $\Omega_{t,i}^{\text{mem}}$ is symmetric positive semidefinite, it admits the eigendecomposition

$$\Omega_{t,i}^{\text{mem}} = U \Lambda U^\top, \quad \Lambda = \text{diag}(\lambda_1, \dots, \lambda_d), \quad \lambda_j \geq 0,$$

where U is orthogonal. Let $y = U^\top x_{t,i}$. From

$$x_{t,i}^+ = (I - \gamma_{\text{mem}} \Omega_{t,i}^{\text{mem}}) x_{t,i},$$

we have

$$U^\top x_{t,i}^+ = (I - \gamma_{\text{mem}} \Lambda) y.$$

Thus, in the eigenbasis of the memory operator, each coordinate is rescaled by $1 - \gamma_{\text{mem}} \lambda_j$.

The weighted energy after protection is

$$\|(\Omega_{t,i}^{\text{mem}})^{1/2} x_{t,i}^+\|_2^2 = \|\Lambda^{1/2} (I - \gamma_{\text{mem}} \Lambda) y\|_2^2 = \sum_{j=1}^d \lambda_j (1 - \gamma_{\text{mem}} \lambda_j)^2 y_j^2.$$

If

$$0 \leq \gamma_{\text{mem}} \leq \frac{1}{\lambda_{\max}(\Omega_{t,i}^{\text{mem}})},$$

then $0 \leq 1 - \gamma_{\text{mem}} \lambda_j \leq 1$ for all j . Hence,

$$\lambda_j (1 - \gamma_{\text{mem}} \lambda_j)^2 y_j^2 \leq \lambda_j y_j^2.$$

Algorithm 1 FOGO: Forgetting-aware Orthogonalization Optimizer

Require: task sequence $\{\mathcal{T}_r\}_{r=1}^T$, learning rate η , weight decay wd, projection Π , hyperparameters, and $\varepsilon > 0$

- 1: Initialize long-term memory $\mathcal{M}_{<1}^{\text{lt}} \leftarrow \emptyset$ and $M \leftarrow \Pi^\top \Pi$
 - 2: **for** task $r = 1, \dots, T$ **do**
 - 3: Initialize $B_0^{(s)}, B_0^{(f)} \leftarrow 0$, active codebook $\mathcal{C}_{r,0}$, and conflict EMA $\bar{r}_0 \leftarrow 0$
 - 4: **for** optimization step $t = 1, \dots, U_r$ **do**
 - 5: $G_t \leftarrow \nabla_{\theta} \mathcal{L}_{\mathcal{T}_r}(\theta)$
 - 6: **Slow-fast streams:** Update $B_t^{(s)}, B_t^{(f)}$; orthogonalize them into $O_t^{(s)}, O_t^{(f)}$; project to $P_t^{(s)} = O_t^{(s)}\Pi$ and $P_t^{(f)} = O_t^{(f)}\Pi$
 - 7: **Geodesic fusion:** Fuse each projected row pair $(P_{t,i}^{(s)}, P_{t,i}^{(f)})$ into $z'_{t,i}$ by SLERP; set $z_{t,i} = \|P_{t,i}^{(s)}\|_2 z'_{t,i}$ and $q_{t,i} = z_{t,i} / (\|z_{t,i}\|_2 + \varepsilon)$
 - 8: **Online memory read and accumulation:** Compare $\{q_{t,i}\}_i$ with the pre-update codebook $\mathcal{C}_{r,t-1}$; assign each query to its nearest centroid and accumulate $(m_{t,j}, s_{t,j})$
 - 9: **Short-term filtering:** Split normalized centroids from $\mathcal{C}_{r,t-1}$ into safe, over-aligned, and conflicting sets; compute $z_{t,i}^{\text{hi}}, z_{t,i}^{\text{conf}}$; update $\gamma_{\text{st},t}$ from \bar{r}_t
 Set $\tilde{z}_{t,i} = z_{t,i} - \gamma_{\text{hi}} z_{t,i}^{\text{hi}} - \gamma_{\text{st},t} z_{t,i}^{\text{conf}}$
 - 10: **Long-term protection:** Let $\mathcal{A}_t^{\text{lt}} \subseteq \mathcal{M}_{<r}^{\text{lt}}$ be the available frozen centroids from previous tasks; form $\tilde{q}_{t,i} = \tilde{z}_{t,i} / (\|\tilde{z}_{t,i}\|_2 + \varepsilon)$
 Activate $\mathcal{B}_{t,i}^{\text{lt}} = \{(\mathcal{T}_\tau, k) \in \mathcal{A}_t^{\text{lt}} : |\langle \tilde{q}_{t,i}, \bar{c}_{\mathcal{T}_\tau, k} \rangle| > \epsilon_{\text{lt}}\}$, where $\tau < r$
 Compute $z_{t,i}^{\text{lt}}$ from $\mathcal{B}_{t,i}^{\text{lt}}$ and set $\bar{z}_{t,i} = \tilde{z}_{t,i} - \gamma_{\text{lt}} z_{t,i}^{\text{lt}}$
 - 11: **Proximal lifting:** Lift $\Delta z_{t,i} = \bar{z}_{t,i} - P_{t,i}^{(s)}$ by $u_{t,i}^{\text{prox}} = (I + 2\lambda M)^{-1}(2\lambda \Delta z_{t,i})$
 Set $\hat{O}_{t,i} = O_{t,i}^{(s)} + \Pi u_{t,i}^{\text{prox}}$
 - 12: **Parameter update:** Stack $\{\hat{O}_{t,i}\}_i$ into \hat{O}_t ; set $\gamma_t = \sigma \sqrt{mn} / (\|\hat{O}_t\|_F + \varepsilon)$
 Update $\theta \leftarrow (1 - \eta \text{wd})\theta - \eta \gamma_t \hat{O}_t$
 - 13: **Codebook flush:** Update EMA statistics $(S_{t,j}, N_{t,j})$ using accumulated $(m_{t,j}, s_{t,j})$; normalize, decorrelate, and re-seed centroids to obtain $\mathcal{C}_{r,t}$
 - 14: **end for**
 - 15: **Consolidation:** Store top- K_r centroids from \mathcal{C}_{r,U_r} as $\mathcal{M}_r^{\text{lt}} = \{(\bar{c}_{\mathcal{T}_r, k}, \nu_{\mathcal{T}_r, k})\}_{k=1}^{K_r}$
 Update $\mathcal{M}_{<r+1}^{\text{lt}} \leftarrow \mathcal{M}_{<r}^{\text{lt}} \cup \mathcal{M}_r^{\text{lt}}$
 - 16: **end for**
 - 17: **return** θ
-

Summing over j gives

$$\|(\Omega_{t,i}^{\text{mem}})^{1/2} x_{t,i}^{\dagger}\|_2^2 \leq \sum_{j=1}^d \lambda_j y_j^2 = \|(\Omega_{t,i}^{\text{mem}})^{1/2} x_{t,i}\|_2^2.$$

Taking square roots gives the desired contraction inequality.

Finally, if $v \in \text{Null}(\Omega_{t,i}^{\text{mem}})$, then $\Omega_{t,i}^{\text{mem}} v = 0$. Therefore,

$$(I - \gamma_{\text{mem}} \Omega_{t,i}^{\text{mem}})v = v.$$

Thus, memory protection contracts the energy measured by the memory operator while leaving directions outside the memory subspace unchanged.

C Detailed Algorithm

We provide the full FOGO algorithm in Algorithm 1, showing how it addresses both short-term and long-term forgetting in standard and continual learning settings.

C.1 Details of Slow–Fast Fusion

We expand the row-wise SLERP operation used in the main text. For $P_{t,i}^{(s)}, P_{t,i}^{(f)} \in \mathbb{R}^d$, define the normalized slow and fast directions

$$\bar{p}_{t,i}^{(s)} = \frac{P_{t,i}^{(s)}}{\|P_{t,i}^{(s)}\|_2 + \varepsilon}, \quad \bar{p}_{t,i}^{(f)} = \frac{P_{t,i}^{(f)}}{\|P_{t,i}^{(f)}\|_2 + \varepsilon}.$$

Let

$$\alpha_{t,i}^{\text{sf}} = \langle \bar{p}_{t,i}^{(f)}, \bar{p}_{t,i}^{(s)} \rangle, \quad \theta_{t,i} = \arccos(\text{clip}(\alpha_{t,i}^{\text{sf}}, -1 + \varepsilon, 1 - \varepsilon)).$$

The tangent direction from the slow stream toward the fast stream is

$$v_{t,i} = \frac{\bar{p}_{t,i}^{(f)} - \alpha_{t,i}^{\text{sf}} \bar{p}_{t,i}^{(s)}}{\left\| \bar{p}_{t,i}^{(f)} - \alpha_{t,i}^{\text{sf}} \bar{p}_{t,i}^{(s)} \right\|_2 + \varepsilon}.$$

Therefore,

$$z'_{t,i} = \cos(\xi \theta_{t,i}) \bar{p}_{t,i}^{(s)} + \sin(\xi \theta_{t,i}) v_{t,i}.$$

The scaled fused update is then obtained as in the main text,

$$z_{t,i} = \|P_{t,i}^{(s)}\|_2 z'_{t,i}.$$

This keeps the slow-stream magnitude while rotating its direction toward the fast stream by a fraction ξ of the slow–fast angle.

C.2 Details of Online Directional Memory

We provide the codebook update details omitted from the main text. After assigning queries to the pre-update codebook, we collect for each centroid j the assigned mass and directional sum:

$$m_{t,j} = \sum_{i=1}^m \mathbf{1}[a_{t,i}^{\text{mem}} = j], \quad s_{t,j} = \sum_{i=1}^m \mathbf{1}[a_{t,i}^{\text{mem}} = j] q_{t,i}.$$

The codebook maintains EMA sufficient statistics,

$$S_{t,j} = \beta_{\text{cb}} S_{t-1,j} + (1 - \beta_{\text{cb}}) s_{t,j}, \quad N_{t,j} = \beta_{\text{cb}} N_{t-1,j} + (1 - \beta_{\text{cb}}) m_{t,j},$$

from which we form a provisional centroid

$$\tilde{c}_{t,j} = \frac{S_{t,j}}{N_{t,j} + \varepsilon}.$$

Codebook decorrelation and re-seeding. To avoid redundant memory slots, we mildly decorrelate each provisional centroid from its most correlated pre-update centroids. Let

$$\hat{c}_{t,j} = \frac{\tilde{c}_{t,j}}{\|\tilde{c}_{t,j}\|_2 + \varepsilon}, \quad \mathcal{R}_{t,j} = \text{TOPR}_{\ell \neq j} |\langle \hat{c}_{t,j}, \bar{c}_{t-1,\ell} \rangle|$$

denote the R previous centroids most correlated with $\hat{c}_{t,j}$. The redundant component is

$$h_{t,j}^{\text{red}} = \sum_{\ell \in \mathcal{R}_{t,j}} \langle \hat{c}_{t,j}, \bar{c}_{t-1,\ell} \rangle \bar{c}_{t-1,\ell},$$

and the updated centroid is

$$c_{t,j} = \frac{\tilde{c}_{t,j} - \lambda_c h_{t,j}^{\text{red}}}{\|\tilde{c}_{t,j} - \lambda_c h_{t,j}^{\text{red}}\|_2 + \varepsilon}.$$

The coefficient λ_c is kept small so that centroids remain faithful to their assigned directions while avoiding redundant slots. Centroids with persistently small usage $N_{t,j}$ are periodically re-seeded from the current queries $\{q_{t,i}\}_{i=1}^m$. Unless stated otherwise, we use $\beta_{\text{cb}} = 0.96$.

C.3 Details of Short-Term Angular-Band Filtering

The main text defines the over-aligned set $\mathcal{H}_{t,i}^{\text{st}}$, the conflicting set $\mathcal{C}_{t,i}^{\text{st}}$, and the resulting short-term correction. Here we provide the weighting and scheduling details. The near-orthogonal safe band is

$$\mathcal{S}_{t,i}^{\text{st}} = \{j : |\langle q_{t,i}, \bar{c}_{t-1,j} \rangle| \leq \epsilon_{\text{st}}\}.$$

Centroids in this set are left unchanged. For the risky sets, we use normalized softmax weights

$$\alpha_{t,i,j}^+ = \frac{\exp(\tau_+ \langle q_{t,i}, \bar{c}_{t-1,j} \rangle)}{\sum_{\ell \in \mathcal{H}_{t,i}^{\text{st}}} \exp(\tau_+ \langle q_{t,i}, \bar{c}_{t-1,\ell} \rangle)}, \quad j \in \mathcal{H}_{t,i}^{\text{st}},$$

$$\alpha_{t,i,j}^- = \frac{\exp(\tau_- |\langle q_{t,i}, \bar{c}_{t-1,j} \rangle|)}{\sum_{\ell \in \mathcal{C}_{t,i}^{\text{st}}} \exp(\tau_- |\langle q_{t,i}, \bar{c}_{t-1,\ell} \rangle|)}, \quad j \in \mathcal{C}_{t,i}^{\text{st}}.$$

If either risky set is empty, its corresponding projected component is set to zero.

Adaptive conflict coefficient. We adapt $\gamma_{\text{st},t}$ according to the energy outside the safe band. For each row,

$$r_{t,i} = \frac{\|z_{t,i}^{\text{conf}}\|_2 + \lambda_{\text{hi}} \|z_{t,i}^{\text{hi}}\|_2}{\|z_{t,i}\|_2 + \varepsilon}, \quad r_t = \frac{1}{m} \sum_{i=1}^m r_{t,i}.$$

We smooth this batch-level conflict signal by EMA,

$$\bar{r}_t = \beta_r \bar{r}_{t-1} + (1 - \beta_r) r_t,$$

and set

$$\gamma_{\text{st},t} = \gamma_{\text{st}}^{\min} + (\gamma_{\text{st}}^{\max} - \gamma_{\text{st}}^{\min}) \frac{\bar{r}_t}{\bar{r}_t + \kappa}.$$

This increases suppression when more update energy lies in risky directions and relaxes it when updates remain near the safe band. Unless stated otherwise, we use fixed temperatures τ_+ , τ_- , EMA decay $\beta_r = 0.95$, and sensitivity $\kappa = 0.20$.

C.4 Details of Long-Term Near-Orthogonal Protection

The main text defines the active protection set $\mathcal{B}_{t,i}^{\text{lt}}$, the protected component $z_{t,i}^{\text{lt}}$, and the final protected update $\bar{z}_{t,i}$. Here we provide the remaining implementation details: candidate selection, importance normalization, and centroid freezing.

Candidate set. At optimization step t of task \mathcal{T}_r , the candidate set $\mathcal{A}_t^{\text{lt}}$ is drawn from the frozen memory

$$\mathcal{M}_{<r}^{\text{lt}} = \bigcup_{\tau < r} \mathcal{M}_{\tau}^{\text{lt}}, \quad \mathcal{M}_{\tau}^{\text{lt}} = \{(\bar{c}_{\mathcal{T}_{\tau},k}, \nu_{\mathcal{T}_{\tau},k})\}_{k=1}^{K_{\tau}}.$$

In practice, $\mathcal{A}_t^{\text{lt}}$ may be the full frozen bank or a compact sampled subset for efficiency. When sampling is used, we sample uniformly or according to normalized importance,

$$p_{\mathcal{T}_{\tau},k} = \frac{\nu_{\mathcal{T}_{\tau},k}}{\sum_{(\mathcal{T}_{\tau'},\ell) \in \mathcal{M}_{<r}^{\text{lt}}} \nu_{\mathcal{T}_{\tau'},\ell} + \varepsilon}.$$

Importance normalization. The weight $\nu_{\mathcal{T}_{\tau},k}$ controls the strength of suppression along a frozen direction. To avoid scale imbalance across tasks, we normalize the weights within each frozen task:

$$\nu_{\mathcal{T}_{\tau},k} \leftarrow \frac{\nu_{\mathcal{T}_{\tau},k}}{\sum_{\ell=1}^{K_{\tau}} \nu_{\mathcal{T}_{\tau},\ell} + \varepsilon}.$$

Centroid selection. At the end of task \mathcal{T}_{τ} , we select K_{τ} centroids from the online codebook using accumulated usage and diversity-adjusted importance. The selected centroids are normalized, stored with their weights in $\mathcal{M}_{\tau}^{\text{lt}}$, and kept fixed during later tasks.

D Detailed Experimental Setup

We provide implementation details for all settings. All experiments are conducted on a cluster equipped with NVIDIA H100 and H200 GPUs and 256-core CPUs, using CUDA 13.0 and PyTorch 2.6. For computationally intensive tasks, we use multi-GPU training: $4\times H200$ for language pre-training and $2\times H200$ for continual fine-tuning. All remaining experiments run on a single GPU. Complete environment specifications and dependencies are provided in the attached code.

D.1 Class-Imbalanced Learning

Datasets. We construct a class-imbalanced variant of CIFAR-10 by designating five classes (4–8) as *rare*, retaining only 10% of their training samples while keeping all samples from the remaining classes. A ResNet-18 is trained from scratch for 50 epochs with batch size 128. We use a learning rate of 10^{-3} for both Adam and FOGO. For Muon, we find this learning rate too small for convergence and increase it to 10^{-2} to match the effective update scale of Adam and FOGO. Results are averaged over ten seeds.

FOGO configuration. We maintain separate codebooks for backbone stages and the classifier head. For the backbone, we use codebook size 96, projection dimension 128, and slow/fast momentum coefficients $\mu_s = 0.97$, $\mu_f = 0.35$, with $K_s = K_f = 5$ Newton–Schulz iterations. The codebook EMA rate is $\beta_{\text{ema}} = 0.95$, and spherical interpolation weight is $\xi = 0.25$. Short-term filtering uses $\epsilon_{\text{st}} = 0.15$, $\gamma_{\text{hi}} = 0.05$, and $\gamma_{\text{st}} \in [0.10, 0.30]$ adapted via $\beta_r = 0.95$ and $\kappa = 0.15$. The decorrelation coefficient is $\lambda_c = 0.10$ with $r = 8$ nearest neighbors. Inactive centroids are re-seeded every 50 optimizing steps at a reset threshold of 0.03. The proximal lifting coefficient is $\lambda_{\text{prox}} = 1.0$ and the update scale is 0.1 for both backbone and head. For the classifier head, we use a codebook size of 64 and a projection dimension of 128.

D.2 Continual Visual Learning

D.2.1 Domain-Incremental Learning.

Datasets. PACS [29] contains 9,991 images of seven shared classes across four domains: Photo, Art Painting, Cartoon, and Sketch. All images are resized to 224×224 and split 80/20 into training and held-out test sets. We fine-tune an ImageNet-pretrained ResNet-18 with frozen batch-normalization statistics for 15 epochs per domain task, using a learning rate of 5×10^{-5} , batch size of 32, and gradient clipping at norm 1.0. Results are averaged over three randomly sampled domain orders and two seeds.

FOGO configuration. We organize FOGO’s memory at the level of semantic network stages rather than individual tensors: separate codebooks are maintained for the stem and each residual stage, while a smaller independent codebook serves the classifier head. Centroids are shared within each stage, but random projections remain tensor-shape specific to accommodate varying dimensions. For the backbone, we use codebook size 64, projection dimension 128, and freeze up to $K_{\text{frz}} = 21$ centroids per stage at each task boundary; for the classifier head, we use codebook size 32, projection dimension 64, and $K_{\text{frz}} = 12$. The slow and fast momentum coefficients are $\mu_s = 0.95$ and $\mu_f = 0.35$ respectively, with $K_s = K_f = 5$ Newton–Schulz iterations and spherical interpolation weight $\xi = 0.3$. Short-term filtering uses $\epsilon_{\text{st}} = 0.15$; long-term protection uses $\epsilon_{\text{lt}} = 0.10$ and $\gamma_{\text{lt}} = 0.6$ for the backbone (0.4 for the head). The codebook EMA rate is $\beta_{\text{ema}} = 0.95$, with inactive centroids re-seeded every 50 steps at a reset threshold of 0.03. Frozen centroids are selected via a drift-aware score combining usage, uniqueness, and movement from the pre-task snapshot, with a larger budget allocated to deeper stages where domain-specific drift is more pronounced. The proximal lifting coefficient is $\lambda_{\text{prox}} = 1.0$, and the update scale is 0.1 for both backbone and head.

Continual learning baselines. When combining with continual learning methods, we use their default hyperparameters: EWC [27] with $\lambda = 5000$, online mode, and 1,024 Fisher samples; ER [6] with buffer size 100, replay batch size 32, and $\alpha = 1.0$; DER++ [4] with buffer size 100, replay batch size 32, $\alpha = 0.1$, and $\beta = 0.5$.

D.2.2 Class Incremental-Learning

Class-Incremental Learning on CIFAR-10. We split CIFAR-10 into five sequential tasks with two classes each: $\{0, 1\}$, $\{2, 3\}$, $\{4, 5\}$, $\{6, 7\}$, $\{8, 9\}$. All images are 32×32 with standard normalization. A ResNet-18 is trained from scratch for 20 epochs per task with learning rate 2×10^{-3} , batch size 128, and gradient clipping at norm 2.0. We use DER++ [4] as the base continual learning framework with a replay buffer of size 200, replay batch size 32, $\alpha = 0.1$, and $\beta = 0.5$, and replace only the optimizer among Adam, Muon, UPGD [10], and FOGO. Results are averaged over five seeds.

FOGO configuration. For class-incremental learning, FOGO organizes memory at the level of semantic network stages. In the backbone, codebooks are shared within each residual stage (stem, layer1–4), while random projections remain tensor-shape specific to handle varying dimensions within a stage. The classifier head uses two separate codebooks: one for the intermediate FC layer (512×512) and a smaller one for the classifier output (10×512 , approximately one centroid per class). This three-tier design—backbone stages, intermediate head, classifier—allows each component to evolve at its natural granularity.

For the backbone, we use codebook size 96, projection dimension 256, slow and fast momentum $\mu_s = 0.97$, $\mu_f = 0.20$, with $K_s = 4$ and $K_f = 4$ Newton–Schulz iterations, and spherical interpolation weight $\xi = 0.20$. The codebook EMA rate is $\beta_{\text{ema}} = 0.96$. Short-term filtering uses $\epsilon_{\text{st}} = 0.25$, $\gamma_{\text{hi}} = 0.01$, and $\gamma_{\text{st}} \in [0.15, 0.40]$ adapted via $\beta_r = 0.95$ and $\kappa = 0.15$. Long-term protection uses $\epsilon_{\text{lt}} = 0.001$ and $\gamma_{\text{lt}} = 1.0$ for both anti-aligned and aligned directions, with a maximum of 48 active frozen centroids sampled per step for efficiency. The decorrelation coefficient is $\lambda_c = 0.05$ with $r = 8$ nearest neighbors. Inactive centroids are re-seeded every 50 steps at a reset threshold of 0.10. The proximal lifting coefficient is $\lambda_{\text{prox}} = 1.0$ and backbone update scale is 0.1.

For the intermediate head FC (512×512), we use codebook size 48, projection dimension 96, and freeze quota of 20 centroids per task. For the classifier (10×512), we use codebook size 12, projection dimension 16, and freeze quota of 8 centroids per task, with $\gamma_{\text{lt}} = 1.0$ and update scale 0.05. The head FOGO learning rate is 5×10^{-4} , and the auxiliary AdamW learning rate for 1D parameters is also 5×10^{-4} .

At each task boundary, FOGO freezes a stage-dependent number of diverse centroids: 20 per backbone stage (stem through layer4), 20 for the intermediate head FC, and 8 for the classifier. Centroids are selected by an importance score that balances usage frequency, directional diversity, and drift from the task-start snapshot.

D.3 Continual Fine-tuning

Datasets. We evaluate on CL4VQA, a sequence of VQA tasks covering distinct reasoning skills (commonsense, location, counting, judgment). The base model is LLaVA-1.5-7B [30] with a frozen CLIP ViT-L/14@336 encoder. We apply MoE-LoRA ($r=16$, $\alpha=16$, 4 experts) to the three MLP modules (gate_proj, up_proj, down_proj). Each task trains for 1 epoch with learning rate 2×10^{-4} (cosine, 3% warmup), effective batch size 32, bfloat16, and sequence length 2048.

FOGO configuration. With rank-16 LoRA, all gradient matrices have $\min(m, n)=16$. We apply the full FOGO pipeline to every LoRA-A and LoRA-B parameter by projecting along its larger dimension, rather than falling back to AdamW for small tensors.

FOGO maintains 9 codebooks ($C=48$, $d=128$), one per combination of depth group (shallow/middle/deep, splitting the 32 LLaMA layers into thirds) and MLP module type. Gate, up, and down projections are separated because their gradient semantics differ (gating vs. expansion vs. compression); a shared codebook would freeze irrelevant directions. All 4 MoE experts at the same depth and module type contribute to a single codebook, enabling cross-expert knowledge transfer. Since LoRA-B is tall (11008×16) while LoRA-A is wide (16×4096), each codebook uses two shape-specific random projections (for $D=4096$ and $D=11008$)—18 projections in total.

The key hyperparameters: dual-stream momentum $\mu_s=0.96$, $\mu_f=0.16$ with 5/4 Newton–Schulz steps and SLERP blend $\xi=0.25$; short-term filter $\epsilon_{\text{st}}=0.20$, $\gamma_{\text{hi}}=0.01$, $\gamma_{\text{st}} \in [0.15, 0.45]$; long-term protection $\epsilon_{\text{lt}}=0.05$, $\gamma_{\text{lt}}=1.0$; proximal coefficient $\lambda_{\text{prox}}=0.8$; update scale $\sigma=0.2$.

At each task boundary, FOGO freezes 23 centroids per codebook, with a larger budget allocated to deeper layers, selected by a score balancing usage, directional uniqueness, and drift from the task-start snapshot.

D.4 Language Pretraining

Datasets. We pretrain GPT-2 Small (125M parameters) from scratch on OpenWebText [13] (~9B training tokens, 4.4M validation tokens) using the nanoGPT implementation [25]. We remove linear-layer biases, use GeLU activations, set dropout to 0.0, replace learned positional embeddings with RoPE [40], and adopt a warmup-stable learning rate schedule [20]. All models are trained for 100K steps on approximately 49.2B tokens, with context length 1024, 2K warmup steps, and an effective batch size of 60 sequences. Architecture, data order, token budget, and all non-optimizer hyperparameters are kept identical across methods.

Baselines. We compare FOGO with Adam [33] and Muon [23]. For Muon-style optimizers, we follow the standard hybrid setup: the orthogonalization-based optimizer is applied to matrix-valued parameters (2D weights), while all remaining parameters (embeddings, biases, layer norms) are updated with Adam. We adopt the same hybrid setup for FOGO. For Adam, we use $(\beta_1, \beta_2) = (0.9, 0.95)$; for Muon, $\beta = 0.95$. Weight decay is set to 0.1 and learning rate to 6×10^{-4} for all methods.

FOGO configuration. For GPT-2, FOGO organizes codebooks by parameter shape, yielding four codebook types shared across all transformer blocks: `c_attn` (768×2304), `c_proj` (768×768), `m1p_fc` (768×3072), and `m1p_proj` (3072×768). Parameters with the same shape share a single codebook, and attention vs. MLP parameters are distinguished via module-type tags. We use codebook size 256 and projection dimension 512, with slow and fast momentum coefficients $\mu_s = 0.95$ and $\mu_f = 0.15$, $K_s = K_f = 5$ Newton–Schulz iterations, and spherical interpolation weight $\xi = 0.25$. The codebook EMA rate is $\beta_{\text{ema}} = 0.96$. Short-term filtering uses $\epsilon_{\text{st}} = 0.20$, $\gamma_{\text{hi}} = 0.001$, and $\gamma_{\text{st}} \in [0.15, 0.30]$ adapted via $\beta_r = 0.95$ and $\kappa = 0.15$. The decorrelation coefficient is $\lambda_c = 0.05$ with $r = 8$ nearest neighbors, and inactive centroids are re-seeded every 200 steps at a reset threshold of 0.10. The proximal lifting coefficient is $\lambda_{\text{prox}} = 1.0$, and the final update scaling follows $\gamma_t = \sigma \sqrt{mn} / (\|\hat{O}_t\|_F + \epsilon)$ with $\sigma = 0.2$. As this is a single-task pretraining setting, long-term protection is inactive. Training is distributed across $4 \times \text{H200}$ GPUs with consistent random projection seeds across ranks.

E More Experimental Results

E.1 Continual Visual Learning

E.1.1 Combining Optimizers with Other Continual Learning Methods

We further examine whether FOGO can complement existing continual learning techniques. We evaluate PACS Domain-IL with two representative approaches: EWC [27], a regularization-based method, and DER++, a replay-and-distillation method. For each method, we replace the optimizer while keeping the continual learning setup fixed.

Table 3 shows that FOGO consistently improves both regularization-based and replay-based continual learning. With EWC, FOGO achieves the highest AP and reduces AF from 7.93% with Muon to 6.26%. With DER++, FOGO attains the best AP and further lowers AF from 3.08% to 2.60%. These gains indicate that directional memory is complementary to existing continual learning mechanisms: EWC and DER++ impose task-level constraints, while FOGO preserves useful update directions at the optimizer level.

E.1.2 Additional Task-Order Results

To further assess the robustness of FOGO, we report additional Class-IL results on CIFAR-10 under different task orders. Beyond the main order used in Fig. 3, we evaluate two alternative sequences: $[[0, 1], [8, 9], [3, 5], [4, 7], [2, 6]]$ and $[[3, 7, 9, 0], [1, 5], [4, 8], [2], [6]]$, covering both balanced and imbalanced class splits. Table 4 shows that FOGO consistently outperforms Adam, Muon, and UPGD across task orders while achieving lower forgetting. This suggests that the gains are not tied to

Table 3: **Combining optimizers with continual learning methods on PACS Domain-IL.** Results are averaged over three randomly selected domain orders and two seeds. AP denotes Average Performance, and AF denotes Average Forgetting. Best results are in bold and second-best results are underlined.

CL Method	Optimizer	Memory	Mem. Usage (MB) ↓	Train Time (m) ↓	AP (%) ↑	AF (%) ↓
EWC	Adam	Fisher	85.3	8.44	83.94 ± 4.26	13.90 ± 6.59
EWC	Muon	Fisher	85.3	<u>9.11</u>	<u>88.57 ± 2.05</u>	<u>7.93 ± 2.65</u>
EWC	CBP	Fisher	85.3	12.85	84.42 ± 1.06	13.56 ± 2.85
EWC	FIRE	Fisher	85.3	11.46	80.44 ± 4.60	14.76 ± 3.68
EWC	FOGO	Fisher + Centroids	<u>85.9</u>	<u>10.98</u>	88.81 ± 3.02	6.26 ± 2.01
DER++	Adam	Buffer + logits	57.4	8.37	92.21 ± 1.18	4.51 ± 0.64
DER++	Muon	Buffer + logits	57.4	<u>8.98</u>	<u>92.86 ± 1.48</u>	<u>3.08 ± 1.01</u>
DER++	CBP	Buffer + logits	57.4	13.90	91.87 ± 1.42	4.66 ± 0.55
DER++	FIRE	Buffer + logits	57.4	11.63	88.12 ± 2.94	6.85 ± 0.25
DER++	FOGO	Buffer + logits + Centroids	<u>58.0</u>	<u>11.02</u>	92.91 ± 2.07	2.60 ± 1.16

Table 4: **Additional CIFAR-10 Class-IL results across different task orders.** AP denotes Average Performance, and AF denotes Average Forgetting. Results are averaged over five random seeds. Best results are in bold and second-best results are underlined.

Task Order	Optimizer	AP (%) ↑	AF (%) ↓
<i>Order 1: balanced two-class increments</i>			
	Adam	38.54 ± 8.41	52.21 ± 6.40
	Muon	26.62 ± 4.21	65.85 ± 3.14
	UPGD	16.37 ± 0.58	63.96 ± 0.93
	FOGO	43.83 ± 5.75	50.32 ± 4.11
<i>Order 2: imbalanced class increments</i>			
	Adam	41.16 ± 7.01	52.94 ± 6.47
	Muon	28.46 ± 2.54	66.54 ± 3.49
	UPGD	20.04 ± 0.08	72.33 ± 0.34
	FOGO	44.45 ± 5.01	52.71 ± 4.97

a favorable class sequence, but reflect the ability of directional memory to preserve task-relevant updates across different incremental learning trajectories.

E.2 Zero-shot OOD Generalization

We further evaluate whether FOGO improves generalization to unseen task types. We finetune LLaVA-1.5-7B with a LoRA-MoE architecture on the first seven VQA tasks, then evaluate the resulting checkpoint zero-shot on the remaining three held-out tasks. As shown in Table 5, FOGO consistently outperforms AdamW and Muon, suggesting that directional memory helps preserve transferable directions for OOD generalization.

F More Analyses and Ablation Studies

F.1 Short-Term Forgetting Analysis

Fig. 1 instruments the class-imbalanced training loop (ResNet-18, CIFAR-10, 5 rare classes at 10% data) with three per-step diagnostics, computed every 10 steps.

Panel (a): Gradient conflict. At each logged step, we compute separate loss gradients for the dominant and rare samples within the current mini-batch and measure their cosine similarity. The cosine remains negative (≈ -0.1) throughout training, indicating that the two groups consistently pull the model in opposing directions. This is the precondition for short-term forgetting: any update that benefits one group risks harming the other.

Table 5: **Zero-shot OOD generalization.** LLaVA-1.5-7B with LoRA-MoE is trained on the first seven VQA task types and evaluated on the last three held-out types without further finetuning. Best results are in bold and second-best results are underlined.

Optimizer	Typ.	Sub.	Cau.
AdamW	57.06	57.98	26.73
Muon	<u>57.80</u>	<u>58.35</u>	<u>29.03</u>
FOGO	59.95	60.47	29.88

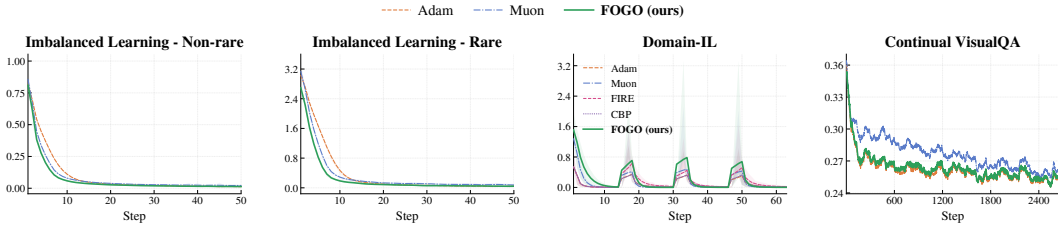


Figure 5: Training loss curves across four continual learning settings. From left to right: class-imbalanced learning on non-rare (dominant) and rare (non-dominant) classes, Domain-IL, and continual VisualQA with LoRA-MoE on LLaVA-1.5-7B. FOGO consistently converges faster and reaches a lower final loss than Adam and Muon across all settings. In Domain-IL, FOGO also outperforms specialized continual learning methods, including FIRE and CBP, and recovers rapidly after each domain shift.

Panel (b): Directional bias. We measure how much the combined gradient (the actual update direction) aligns with each group by projecting it onto the dominant and rare gradient directions. During steps 0–200, the projection onto the dominant group is high (~ 0.85) while the rare group is low (~ 0.3): the optimizer primarily serves the dominant group. After step ~ 200 , the pattern reverses—dominant samples have largely converged, their per-sample gradients shrink, and the rare group’s larger gradients take over the combined update direction. This mirrors the subspace rotation described in Corollary 2: whichever group does not control the dominant subspace of B_t has its directions suppressed.

Panel (c): Direct forgetting evidence. To confirm that gradient conflict translates into actual loss degradation, we measure $\Delta L = L(\theta_{t+1}) - L(\theta_t)$ on a *fixed held-out probe* of 256 samples per group, evaluated before and after each parameter update. During the dominant-serving phase (steps 0–200), the rare group’s validation loss increases by up to $+0.10$ per step—direct evidence that the suppressed group is being harmed. After the directional bias reverses, the dominant group exhibits a persistent positive ΔL , confirming that short-term forgetting shifts between groups as the optimization trajectory evolves. The use of held-out data rules out batch-level memorization as an explanation.

F.2 Training Behaviors

To comprehensively study the training dynamics of FOGO, we include the training loss curves across three settings in Fig. 5.

Class-Imbalanced Learning. The first two panels of Fig. 5 show the per-class training loss on the non-rare and rare partitions, respectively. FOGO converges noticeably faster than both Adam and Muon within the first 5 steps and maintains a consistently lower loss throughout training. The advantage is especially pronounced on the rare classes, where the loss gap between FOGO and the baselines remains significant even after convergence, indicating that the gradient correction mechanism of FOGO is particularly effective for under-represented classes.

Domain-Incremental Learning. The third panel presents the training loss under domain-incremental learning, where the model encounters a sequence of domains. All methods exhibit

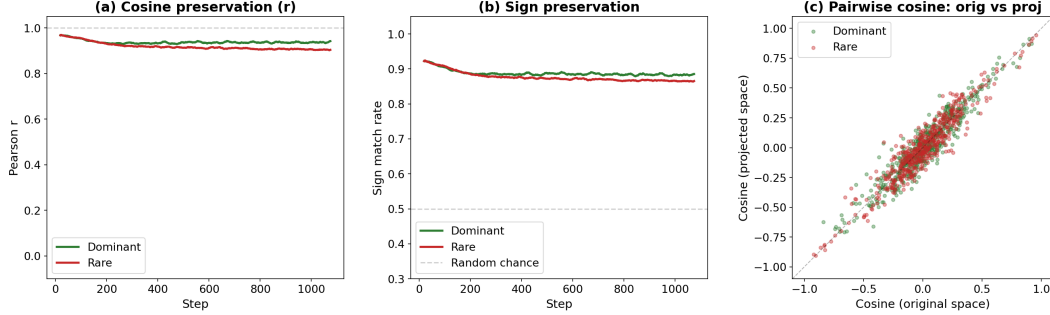


Figure 6: **Gradient structure preservation under random projection** (CIFAR-10, ResNet-18, $d=128$). **(a)** Pearson correlation between pairwise cosine similarities in the original and projected spaces remains above 0.9 for both groups. **(b)** Sign preservation rate stays around 89%, well above the 50% random baseline. **(c)** Scatter of individual cosine pairs at the final training step; both groups cluster tightly around the $y=x$ identity line. Dominant and rare groups show nearly identical fidelity, confirming that projection quality is independent of subgroup sample size.

periodic loss spikes at domain boundaries, as expected. However, FOGO recovers substantially faster after each transition compared to both standard optimizers (Adam, Muon) and dedicated continual learning baselines (FIRE, CBP), demonstrating its robustness to distributional shifts.

Continual VisualQA. The rightmost panel shows the training loss when integrating FOGO into LoRAMoE with LLaVA-1.5-7B for continual visual question answering. Despite the increased model complexity, FOGO achieves a lower and more stable training loss throughout, confirming that its benefits generalize beyond standard classification to multi-modal generative settings.

F.3 Gradient Structure Preservation under Random Projection

A central design choice in FOGO is the use of a random Rademacher projection $\Pi \in \mathbb{R}^{n \times d}$ to map each layer’s gradient matrix from the original parameter space (\mathbb{R}^n) to a lower-dimensional codebook space (\mathbb{R}^d , $d \ll n$). For the downstream codebook operations to be meaningful, this projection must preserve the pairwise geometric structure of gradient directions—if two gradient rows are aligned or conflicting in the original space, they should remain so after projection.

We verify this empirically on the class-imbalanced CIFAR-10 benchmark (see Section 5.1). At each training step, we compute the pairwise cosine similarities between gradient row vectors within each layer, both in the original n -dimensional space and in the d -dimensional projected space ($d=128$). We then measure Pearson correlation between the two sets of cosines and the rate at which projection preserves the sign of each pairwise cosine. To ensure that this property is not an artefact of data abundance, we report results separately for the dominant group (8 classes, full data) and the rare group (2 classes, 10% data).

Fig. 6 summarizes the results. The Rademacher projection preserves pairwise cosine structure with Pearson $r > 0.9$ throughout training for both groups, and sign fidelity remains around 89%. Crucially, the two groups exhibit nearly identical preservation quality despite a $\sim 10\times$ difference in sample count, confirming that the projection is data-agnostic: it neither favors nor disadvantages any subgroup. The scatter plot further shows that deviations from perfect preservation concentrate near cosine ≈ 0 (near-orthogonal pairs), where the practical impact on interference detection is minimal. These results justify FOGO’s use of random projection as a faithful dimensionality reduction step that retains the gradient geometry needed for codebook-based conflict management.

F.4 Short-Term Forgetting in Continual Learning

We ablate short-term angular-band filtering while keeping all other components of FOGO unchanged. As shown in Table 6, enabling this module improves AP from 87.37% to 87.89% and reduces AF from 6.90% to 6.77%. The improvement is modest but consistent, indicating that short-term filtering helps reduce local interference during training. In PACS Domain-IL, however, the main retention effect

Table 6: **Effect of short-term filtering on PACS Domain-IL.** Results are averaged over three randomly selected domain orders and two seeds. AP denotes Average Performance, and AF denotes Average Forgetting.

Method	ST Filtering	AP (%) \uparrow	AF (%) \downarrow
FOGO w/o ST filtering	Disabled	87.37 \pm 4.23	6.90 \pm 2.48
FOGO	Enabled	87.89 \pm 2.94	6.77 \pm 2.31

appears to come from long-term centroid protection, while short-term filtering provides additional stabilization.

F.5 Efficiency Analysis

F.5.1 Theoretical Algorithm Complexity

We analyze the per-step cost for one matrix-shaped update block $G_t \in \mathbb{R}^{m \times n}$. Let d denote the projected memory dimension, with $d \ll n$ and typically $d \ll \min\{m, n\}$. Adam performs elementwise moment updates and costs $\mathcal{O}(mn)$. Muon adds Newton–Schulz orthogonalization; with K_{NS} iterations, its dominant cost is

$$\mathcal{O}(K_{\text{NS}}mn \min\{m, n\}).$$

FOGO maintains slow and fast orthogonalized streams, giving a constant-factor overhead over Muon:

$$\mathcal{O}(2K_{\text{NS}}mn \min\{m, n\}).$$

The remaining operations are performed in the projected space \mathbb{R}^d . Computing the two projections $P_t^{(s)} = O_t^{(s)}\Pi$, $P_t^{(f)} = O_t^{(f)}\Pi$, and the final lifting $\Pi u_{t,i}^{\text{prox}}$ costs $\mathcal{O}(3mnd)$ for a dense projection. The online memory read, including nearest-centroid assignment, costs $\mathcal{O}(mCd)$, where C is the active codebook size. Short-term angular-band filtering reuses the codebook similarities and accumulates the over-aligned and conflicting projected components, costing at most another $\mathcal{O}(mCd)$. Long-term protection compares against K_{cand} sampled frozen centroids and accumulates the protected component, costing $\mathcal{O}(2mK_{\text{cand}}d)$. With $M = \Pi^\top \Pi$ precomputed, the proximal solve costs $\mathcal{O}(md^2)$. Thus, the per-step cost is

$$\mathcal{O}(2K_{\text{NS}}mn \min\{m, n\} + 3mnd + 2mCd + 2mK_{\text{cand}}d + md^2).$$

The projected-memory overhead relative to the dual-stream orthogonalization term is

$$\frac{3mnd + 2mCd + 2mK_{\text{cand}}d + md^2}{2K_{\text{NS}}mn \min\{m, n\}} = \frac{d(3n + 2C + 2K_{\text{cand}} + d)}{2K_{\text{NS}}n \min\{m, n\}}.$$

Hence, when $d, C, K_{\text{cand}} \ll \min\{m, n\}$, the forgetting-aware memory correction is lower order than the orthogonalization cost. The dominant overhead over Muon is therefore the intentional slow–fast dual stream, while the short-term and long-term memory operations remain comparatively small.

The optimizer-state memory is

$$\mathcal{O}(2mn + Cd + K_{\text{lt}}d + d^2),$$

assuming the random projection is generated implicitly from a seed. The $2mn$ term stores the slow and fast momentum states, while Cd , $K_{\text{lt}}d$, and d^2 correspond to the active codebook, frozen centroids, and proximal matrix $M = \Pi^\top \Pi$, respectively. If Π is stored explicitly, an additional $\mathcal{O}(nd)$ term is required. Thus, FOGO is heavier than Adam and Muon, but its forgetting-aware memory scales with the projected dimension d , not the full update dimension.

F.5.2 Overhead FLOPs

We next give a concrete FLOP-level estimate to contextualize the overhead. This estimate counts dominant matrix operations and ignores small elementwise costs, so it should be interpreted as an order-of-magnitude comparison rather than an exact wall-clock predictor.

Consider a square block with $m = n = 4096$, projection dimension $d = 512$, codebook size $C = 384$, sampled frozen centroids $K_{\text{cand}} = 64$, and $K_{\text{NS}} = 5$. Muon’s dominant cost comes from Newton–Schulz orthogonalization:

$$K_{\text{NS}}mn \min\{m, n\} = 5 \cdot 4096^3 \approx 3.44 \times 10^{11}.$$

FOGO applies orthogonalization to both slow and fast streams, giving

$$2K_{\text{NS}}mn \min\{m, n\} = 2 \cdot 5 \cdot 4096^3 \approx 6.87 \times 10^{11}.$$

The projected-space overhead is substantially smaller. Projection and lifting cost

$$3mnd = 3 \cdot 4096^2 \cdot 512 \approx 2.58 \times 10^{10}.$$

Online codebook lookup costs

$$mCd = 4096 \cdot 384 \cdot 512 \approx 8.05 \times 10^8.$$

Short-term angular-band filtering reuses the codebook similarities and accumulates the over-aligned and conflicting projected components, costing at most another

$$mCd \approx 8.05 \times 10^8.$$

Long-term protection over sampled frozen centroids costs approximately

$$2mK_{\text{cand}}d = 2 \cdot 4096 \cdot 64 \cdot 512 \approx 2.68 \times 10^8,$$

where the factor 2 accounts for alignment computation and protected component accumulation. Finally, the proximal solve costs

$$md^2 = 4096 \cdot 512^2 \approx 1.07 \times 10^9.$$

Thus, the additional projected-space operations contribute approximately

$$2.58 \times 10^{10} + 8.05 \times 10^8 + 8.05 \times 10^8 + 2.68 \times 10^8 + 1.07 \times 10^9 \approx 2.87 \times 10^{10}.$$

This is about

$$\frac{2.87 \times 10^{10}}{6.87 \times 10^{11}} \approx 4.2\%$$

of the dual-stream orthogonalization cost. Therefore, for $d = 512$, the main overhead over Muon comes from using two orthogonalized streams, while the forgetting-aware memory mechanism itself adds only a modest projected-space cost.

Compared with Adam, FOGO is significantly more expensive because it is not an elementwise optimizer. Compared with Muon, the overhead is more controlled: the dominant increase is the slow–fast dual stream, and the short-term and long-term memory terms scale with d , C , and K_{cand} , rather than the full block dimension. This makes the extra cost acceptable when explicit control of short-term and long-term forgetting is the goal.

F.5.3 Training Time and Memory Usage

We evaluate the practical efficiency of FOGO across all experimental settings. Table 7 reports wall-clock training time, peak GPU memory allocation, and persistent method memory. The latter isolates the storage required for forgetting control, such as replay buffers, stored models, or centroid memories, from transient GPU memory used during training.

Overall, FOGO introduces only a modest increase in peak GPU memory across settings, while requiring a small amount of persistent memory for its centroid state. The overhead is more visible in smaller vision experiments, where the baseline runtime is short, but remains moderate relative to the full training cost in large-scale GPT-2 pretraining and Continual VisualQA. Notably, the persistent memory of FOGO remains compact: it avoids storing replay data or previous model snapshots, and instead maintains only lightweight directional centroid memories for forgetting control.

Table 7: **Training time and memory usage across evaluation settings.** We report wall-clock training time, peak GPU memory allocation, and persistent method memory. Method memory denotes storage used for replay buffers, stored models, or centroid memories, separate from transient GPU memory.

Benchmark	Method	Training Time (mins)	GPU Memory (GiB)	Method Memory (MB)
Class-imbalanced	Adam	6.51	1.85	–
	Muon	7.75	1.85	–
	FOGO	11.91	1.91	–
GPT-2 pretraining	Adam	844*	79.65	–
	Muon	890*	79.70	–
	FOGO	964*	79.98	–
Class-IL	Adam	5.51	2.10	2.35
	Muon	6.62	2.11	2.35
	FOGO	10.08	2.39	2.80
Continual VisualQA	AdamW	605.0 [†]	56.08	< 0.1
	Muon	626.0 [†]	56.15	< 0.1
	FOGO	857.4 [†]	59.95	36.7

*Training uses 4 GPUs. [†]Training uses 2 GPUs. For Continual VisualQA, GPU memory is measured on the Judge task; relative memory differences are similar across tasks. “–” indicates no additional persistent method memory, and < 0.1 MB denotes negligible storage for data-free methods.

F.6 Expert Representation Geometry in Continual VisualQA

We further analyze why FOGO outperforms other optimizers in continual VisualQA by visualizing expert activations after training on a sequence of tasks. Figure 7 compares the representation geometry induced by FOGO and AdamW. To make the comparison independent of routing frequency, both plots use the same number of sampled points per expert.

AdamW produces a highly imbalanced representation space. As shown in Figure 7b(b), one expert collapses into a narrow region, while the remaining experts cover broader and more scattered feature regions. This suggests uneven expert utilization at the representation level: collapsed experts become overly specialized and lose plasticity, whereas high-variance experts must absorb heterogeneous task patterns. In a continual learning setting, such imbalance is harmful because new tasks are likely to overwrite the broadly activated experts, while collapsed experts contribute little to future adaptation.

In contrast, FOGO yields a more balanced expert geometry, as shown in Figure 7a(a). The expert clusters remain well separated while preserving comparable within-expert diversity. This indicates that FOGO distributes task-related variation more evenly across experts, avoiding both feature collapse and excessive dispersion. Such balanced variance provides a more favorable stability–plasticity trade-off: each expert retains enough capacity to adapt to new VisualQA tasks without concentrating the burden of continual updates on only a small subset of experts.

G Case Study and Qualitative Analysis

In this section, we present a qualitative comparison between the baseline LoRA-MoE trained continually with AdamW and our proposed FOGO model across various VisualQA scenarios. We selected four representative cases to demonstrate FOGO’s superiority in fine-grained recognition, scene understanding, counting, and reasoning.

As illustrated in Figure 8, FOGO outperforms the baseline in several key dimensions:

- **Specificity in Recognition:** In the pizza example (Fig. 8a), while LoRA-MoE provides a generic category (“Greens”), FOGO correctly identifies the specific ingredient (“Spinach”), showcasing superior fine-grained visual capabilities.
- **Holistic Scene Interpretation:** For the market scene (Fig. 8b), FOGO delivers a comprehensive summary (“Fruit”) rather than focusing on a single item (“Apples”), reflecting a better grasp of global context.
- **Numerical Precision:** FOGO accurately counts the objects in the tower (Fig. 8c), whereas LoRA-MoE fails to detect all relevant targets in the counting task.

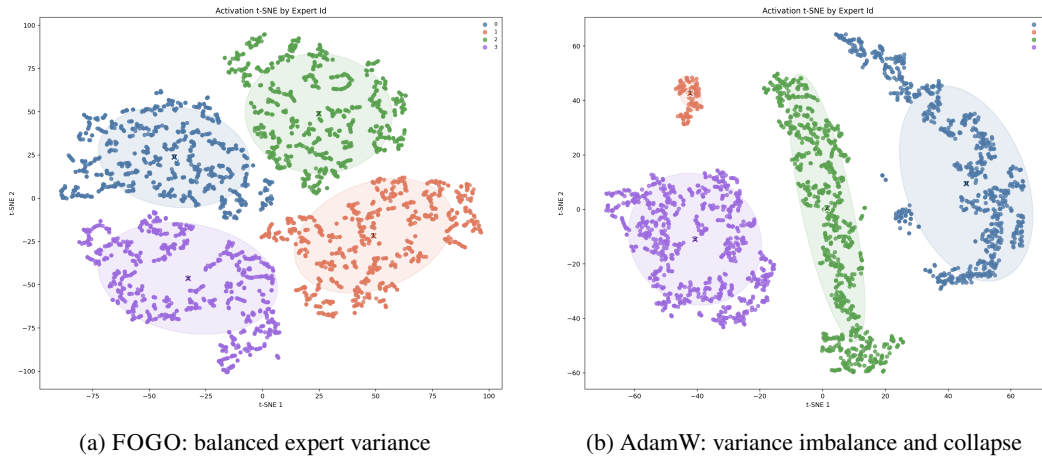


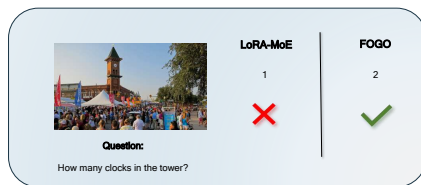
Figure 7: **t-SNE visualization of expert activations in continual VisualQA.** Both plots use the same number of sampled points per expert, isolating representation geometry from routing-load differences. **(a)** FOGO maintains balanced within-expert variance and clear expert separation, suggesting a healthier distribution of task-specific representations. **(b)** AdamW leads to representation imbalance, where one expert collapses into a narrow region while others cover scattered high-variance features, increasing susceptibility to forgetting under sequential task learning.



(a) Fine-grained Recognition



(b) Scene Context Understanding



(c) Visual Counting



(d) Commonsense Reasoning

Figure 8: Qualitative comparison between LoRA-MoE and FOGO. FOGO consistently provides more precise, context-aware, and logically sound answers.

- **Logical Reasoning:** In response to why the horses’ feet are white (Fig. 8d), FOGO moves beyond tautological descriptions (“They are white”) to provide a commonsense-based causal explanation (“Born that way”).

H Limitation and Future Work

FOGO requires specifying a codebook size and projection dimension; we derive principled defaults from the Johnson–Lindenstrauss bound and find them stable across all our settings, though they may benefit from adaptive tuning for very long task sequences. The codebook capacity is currently fixed and cannot yet grow or compress in response to changing task complexity. Additionally, spectral orthogonalization and codebook maintenance introduce modest computational overhead compared to Adam; we find this acceptable given the consistent gains, but further engineering—such as reduced-frequency codebook updates—could narrow the gap. More broadly, we believe a complete solution to forgetting requires joint effort across optimization, architecture, and data strategy; FOGO addresses the first axis and is designed to complement advances in the other two. Promising future directions include dynamic codebook sizing, adaptive projection dimensions, and extension to fully boundary-free continual learning.